

GROWTH AND PROPERTIES OF SPRAYED IRON
DISULFIDE(FeS₂) THIN FILM

By

LONA NDJELI

UNIVERSITY OF NAIROBI
CHIEFOMO LIBRARY

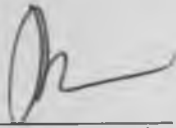
THIS THESIS HAS BEEN ACCEPTED FOR
THE DEGREE OF MSc 1997
AND A COPY MAY BE
UNIVERSITY OF NAIROBI
ED IN THE

A Thesis submitted to the University of Nairobi in partial
fulfillment of the requirements for the degree of Master of Science

1997

DECLARATION

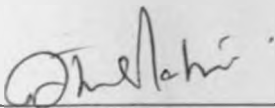
This thesis is my original work and has not been presented for a degree in any other University.



LONA Ndjeli

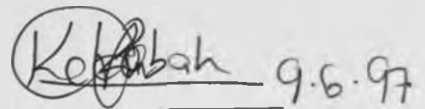
University of Nairobi

This thesis has been submitted for examination with the approval of my University Supervisors:



1. Dr. A. K. Raturi

Department of Physics
University of Nairobi.



2. Dr. K. Rabah

Department of Physics
University of Nairobi.

To my family

ACKNOWLEDGMENT

I would like to express my sincere gratefulness to my supervisors Dr. A. Raturi and Dr. K. Rabah for their guidance, suggestions and encouragements during the period of this research. I am heartily thankful for their support even when matters seemed to be at their worst. The same gratitude goes to Prof. R. C. Genga, Head of the Department, for his needed encouragements and moral support for the completion of this work.

Grateful acknowledgement is made to the Physics, Chemistry and Biochemistry Departments of the University of Nairobi for the unfailing assistance of their technical staff and the laboratory facilities.

Thanks to my family for the patience and understanding they have showed me during the course of this work. Thanks also to my colleagues and all those who have contributed towards this project.

Above all, I must express my indebtedness to Deutscher Akademischer Austauschdienst (DAAD) for the scholarship which made this work financially and materially possible.

CONTENTS

Acknowledgement	(i)
Contents	(ii)
Abstract	(iv)
Illustrations and Tables	(v)
List of symbols	(vii)
Chapter one: Introduction	1
1.1 Primary Energy Sources	1
1.2 Solar Radiation	2
1.2.1 Solar Spectrum	2
1.2.2 Sunlight Conversion	6
1.3 Solar Cells.....	6
1.3.1 Introduction.....	6
1.3.2 Types of Solar Cells: Crystalline Silicon vs Thin Film	7
1.3.3 Solid State Solar Cells	10
1.3.4 Semiconductor-electrolyte based Cells (Wet Cells). ..	11
1.4 Materials for Wet Solar Cells	20
1.5 Objectives	25
Chapter two: Theoretical Background	26
2.1 Iron Pyrite Crystal	26
2.2 Band Structure of Solids	26
2.3 Electronic Structure of Iron Pyrite	28
2.4 Photoelectrochemical Mechanism	31
2.5 Thin Films Growth	32

2.6 Stresses and Defects in Thin Films	38
2.7 Charge Carriers Scattering	40
2.8 Direct and Indirect Transitions	41
2.9 Absorption Coefficient	44
2.10 Transmission and Reflection	45
2.11 Resistivity and Hall Effect	46
Chapter three: FeS₂ Films Growth	51
3.1 Spray Pyrolysis	51
3.2 Experimental Set-up	52
3.3 Film Preparation	54
3.4 Heat Treatment	55
3.5 Some Qualitative Observations	56
Chapter Four: Results and Discussion	58
4.1 Thickness	58
4.2 Surface Morphology	59
4.3 Crystallographic Properties	61
4.4 Optical Properties	63
4.5 Electrical Properties	72
Chapter Five: Conclusion and Suggestions	78
5.1 Conclusion	78
5.2 Suggestions	80
References	82

ABSTRACT

Recently, iron pyrite (FeS_2) has been considered as a potential material for thin film solar cells and wet cells. In the present work pyrite FeS_2 films have been grown by spray pyrolysis followed by sulfidation.

The deposition parameters were identified and their optimum values determined. The following values were found: temperature $\approx 500^\circ\text{C}$, spray rate $\approx 24 \text{ cm}^3/\text{min}$, and substrate to sprayer nozzle distance ≈ 35 to 40 cm . The contents $\text{FeCl}_3:\text{CS}(\text{NH}_2)_2:\text{H}_2\text{O}$ of the spraying mixture were found to be in the volume ratios $0.07:0.15:0.78$ for molarities in the range 0.1 and 1 while for molarities less than 0.1 the volume ratios were $1:2$.

Transmission data analysis in the wavelength range $0.4 \mu\text{m}$ and $0.8 \mu\text{m}$ gave an indirect energy gap $\approx 1.17 \text{ eV}$, a possible direct band gap $\approx 2.60 \text{ eV}$ and an absorption coefficient $\approx 10^4 \text{ cm}^{-1}$. Sulfidated samples showed absorption coefficient of $\approx 10^5 \text{ cm}^{-1}$. The structural analysis revealed an improvement in the crystallization with the increasing sulfidation temperature. The films showed a preferred orientation in the (200) direction. Electrical transport properties study indicated that the films exhibit n-type conduction. The carrier concentration was found to be $n \approx (0.15 - 0.23) \times 10^{17} \text{ cm}^{-3}$, the Hall mobility $\mu_H \approx 0.6$ to $1.5 \text{ cm}^2 \text{ V}^{-1} \text{ s}^{-1}$ and the Hall constant $R_H \approx (-4.2$ to $-2.3) \times 10^2 \text{ cm}^3 \text{ C}^{-1}$.

ILLUSTRATIONS AND TABLES.

Fig.1.1 The three components of the solar radiation in the atmosphere 4

Fig.1.2 The air mass 4

Fig.1.3 The solar spectrum 5

Fig.1.4 Different steps in silicon production from sand 8

Fig.1.5 Contact barrier potential formation at a solid state junction 13

Fig.1.6 Two days operation of an n-Cd(Se,Te)/aqueous Cs₂S_x/SnS PEC cell with in-situ storage 13

Fig.1.7 A possible structure of a PEC cell 15

Fig.1.8 The electric double layer and, the distribution of spatial charge q and potential ϕ at an n-type semiconductor-electrolyte interface 18

Fig.2.1 Crystal structure of iron pyrite FeS₂ 27

Fig.2.2 Schematic representation of the bands in iron pyrite .. 30

Fig.2.3 Energy band diagram of an n-type semiconductor/electrolyte/metal system before physical contact 33

Fig.2.4 Energy band diagram of an n-type semiconductor/electrolyte/metal system after physical contact at equilibrium and at zero bias in dark 33

Fig.2.5 Energy band diagram of a wet cell under illumination .. 34

Fig.2.6 Flow of charge carriers around a circuit of a PEC cell in series with a load 34

Fig.2.7 Potential of interaction between the substrate and the striking atom 37

Fig.2.8 Edge dislocation	39
Fig.2.9 Screw dislocation	39
Fig.2.10 Energy band structure of Ge, Si and GaAs	43
Fig.2.11 Energy-crystal momentum relationship	43
Fig.2.12 Experimental set up for Hall measurement	50
Fig.3.1 Experimental set-up for spray pyrolysis	53
Fig.4.1 Scanning electron micrograph	60
Fig.4.2 X-ray diffractograph	62
Fig.4.3 Transmission spectra	66
Fig.4.4 Absorption coefficient as function of wavelength	67
Fig.4.5 Plot of $(\alpha h\nu)^{1/2}$ as function of photon energy	70
Fig.4.6 Plot of $(\alpha h\nu)^2$ as function of photon energy	71
Fig.4.7 Sheet resistance as function of temperature	76
Fig.4.8 Plot of $\ln R_s$ as a function of temperature ⁻¹	77
Table 3.1 Volume ratio of the spraying solution components	55
Table 4.1 Transmittance as a function of wavelength	64
Table 4.2 Absorption coefficient	65
Table 4.3 Values of $(\alpha h\nu)^{1/2}$ and $(\alpha h\nu)^2$ as function of photon energy	68
Table 4.4 Hall constant	73
Table 4.5 Carriers concentration and Hall mobility	75

LIST OF SYMBOLS

AM	air mass
E_c	bottom of the conduction band
E_f	Fermi level
E_g	energy band gap
E_v	top of the valence band
ff	fill factor
h, \hbar	Plank's constants
I_0	dark saturation current
I_{sc}	Short circuit current
k	Boltzman constant
MV	methylviologen
n, p	electrons and holes concentration
PEC	Photoelectrochemical
R_s	sheet resistance
V_{oc}	open circuit voltage
V_{redox}	redox potential
α	absorption coefficient
η	efficiency
μ	carrier mobility
ν, ω	photon frequency
ρ	resistivity
τ	lifetime
ϕ, Φ	potential, work function
χ	electron affinity
Ω, E_p	phonon frequency, phonon energy

CHAPTER ONE

INTRODUCTION

1.1. Primary Energy Sources.

Energy demand is rapidly growing throughout the world under the pressure of increasing industrialization and population growth. The electrical power is increasingly needed by rural communities throughout the world, for sustainable development and decent quality of life. As energy production systems are selected to meet these needs, the environmental ramifications of the generating systems become increasingly important. There is a need for generating energy without emitting greenhouse gases, as this results in global air quality advantages. Apart from supplying sparsely populated areas, there are more complicated energy demands like supplying satellites and deep-sea exploration vehicles with power. Transmission lines cannot be used in these cases and therefore there is need to generate electricity where it is required.

The actually known energy sources can be classified into two groups: energy capital and energy income [1]. The energy capital consists of fossil and nuclear fuels and the energy income refers to renewable resources such as wind, tides, rivers, radiation, steam and biomass. Fossil energy sources and most of renewable energy reserves depend on the sun as the primary source [2]. The only energy sources that are not derived from solar energy are nuclear, geothermal and tidal energy.

The world's present energy is mostly provided by the capital sources. Power is mainly produced in the form of heat and electricity by burning fossil fuel or using potential energy of water. The limited availability of fossil and nuclear fuels - their environmental impacts and the high capital cost needed to produce electricity by traditional method - have led to a growing interest in the renewable energy sources. Among these sources, solar radiation offers the hope of promoting a sustainable development and a decent quality of life for humankind.

1.2. Solar Radiation.

1.2.1. Solar Spectrum.

The radiative energy out put from the sun is enormous: the earth's surface receives an average of about 1.2×10^{17} W of solar power [3]. This means that in less than one hour, enough energy is supplied to the earth to satisfy the entire energy demand of the human population over the whole year.

The solar spectrum outside of the earth's atmosphere is different from the spectrum at the earth's surface. This is due to scattering and absorption inside the atmosphere. Fig. 1.1 shows the three components of the global radiation reaching a receiver on the ground. The three component are the beam (direct) radiation, the diffuse (scattered) radiation and the albedo (reflected radiation). The degree by which the atmosphere affects the sunlight received at the earth's surface is characterized by the air mass. The air mass

is the ratio of the actual path length of solar radiation through the atmosphere to its minimum. On a clear day at sea level, the radiation from the sun corresponds to the air mass one (AM1). When the sun is not at zenith, the air mass is approximately given by:

$$\text{air mass} = 1/\cos\theta_z$$

where θ_z is the zenith angle as shown on Fig. 1.2.

The extraterrestrial spectrum is denoted by AM0 and corresponds to a total incident integrated power i.e. irradiance $S = 1367 \text{ W/m}^2$. The standard sunlight at the earth's surface on a clear day is AM 1.5. It corresponds to a zenith angle $\theta_z = \cos^{-1}(1/1.5)$ and an irradiance of 1 kW/m^2 .

Meanwhile, the available power is less than this due to the weather conditions and the rotation of the earth. As the air mass increases the attenuation of the light becomes stronger as the diffuse light component becomes larger. Fig. 1.3 shows the solar spectrum; indicated are the commonly used air mass spectra and the black body spectrum.

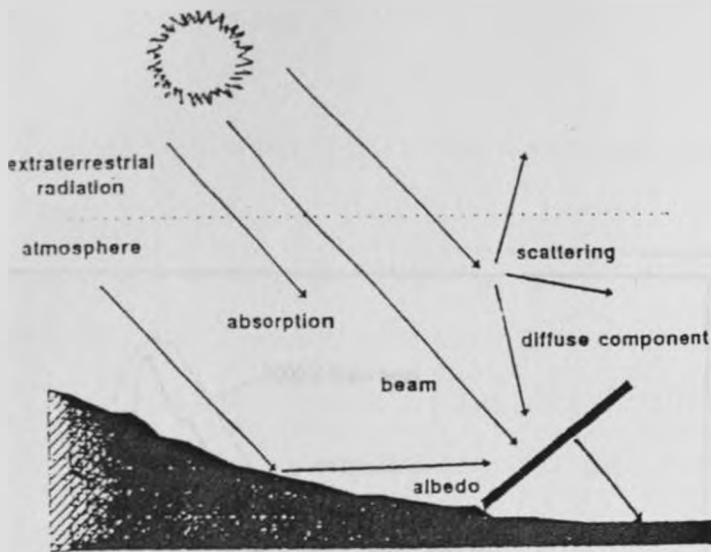


Fig.1.1.1. The three components of solar radiation in the atmosphere.

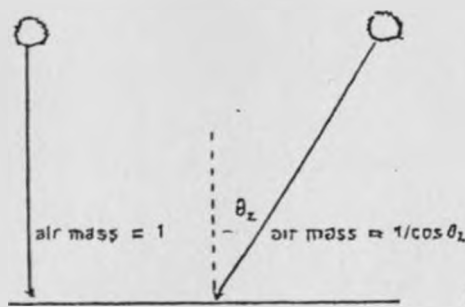
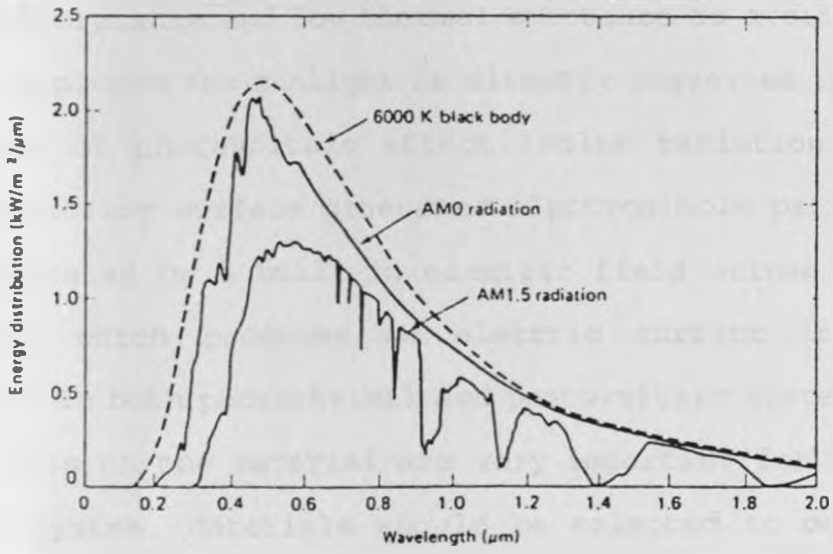


Fig.1.1.2. The air mass.



Spectral distribution of sunlight.

Fig. 1.3. Solar spectrum [4].

1.2.2. Sunlight Conversion.

Several methods of utilizing solar radiation are being used or tested today. They can be divided into two categories: photothermal and photovoltaic conversions.

In the photothermal approach, sunlight is absorbed by a specially designed surface to generate heat. The surface should have high solar absorptance and low thermal emittance to avoid losses. In the second approach the sunlight is directly converted into electricity by means of photovoltaic effect. Solar radiation incident on a semiconducting surface generates electron-hole pairs. These pairs are separated by a built-in electric field across the solar cell junction which produces an electric current in the external circuit. In both photothermal and photovoltaic systems, the optical properties of the material are very important for the performance of the system. Materials should be selected to obtain low cost, long life, efficient and reliable devices.

1.3. Solar Cells.

1.3.1. Introduction.

At present, solar cells are not competitive with other means of generating electricity for terrestrial use but, their long-run potential has attracted increasing attention. There is an extensive range of applications where it is already viewed as the best option for electricity supply; namely, rural electrification, water pumping and satellite power systems. All these applications exploit

the fact that solar radiation is non-polluting and cost effective; the equipment can operate unattended, is very reliable and requires little maintenance.

Research and development in the field of photovoltaic energy conversion are directed at developing materials of improved characteristics and low cost manufacturing techniques.

1.3.2 Types of Solar Cells: Crystalline Silicon versus Thin Film.

Until recently, the chief candidate material for solar cell application has been crystalline silicon. Pure silicon is obtained from sand (SiO_2) through tedious transformation process described in Fig. 1.4. Monocrystalline as well as multicrystalline silicon are used to make cost effective photovoltaic cells. The conversion efficiencies exceeding 30% have been reported in laboratory but the typical efficiencies for commercial devices are 10-15% [3]. Highly efficient but expensive cells are also made from single crystalline silicon and compound semiconductor for specialized applications like electric power generation in space [1].

Crystalline silicon based cell- and module-fabrication technology is well developed and the most reliable at the present time. However it requires sophisticated equipment and complex technological processes [3-5].

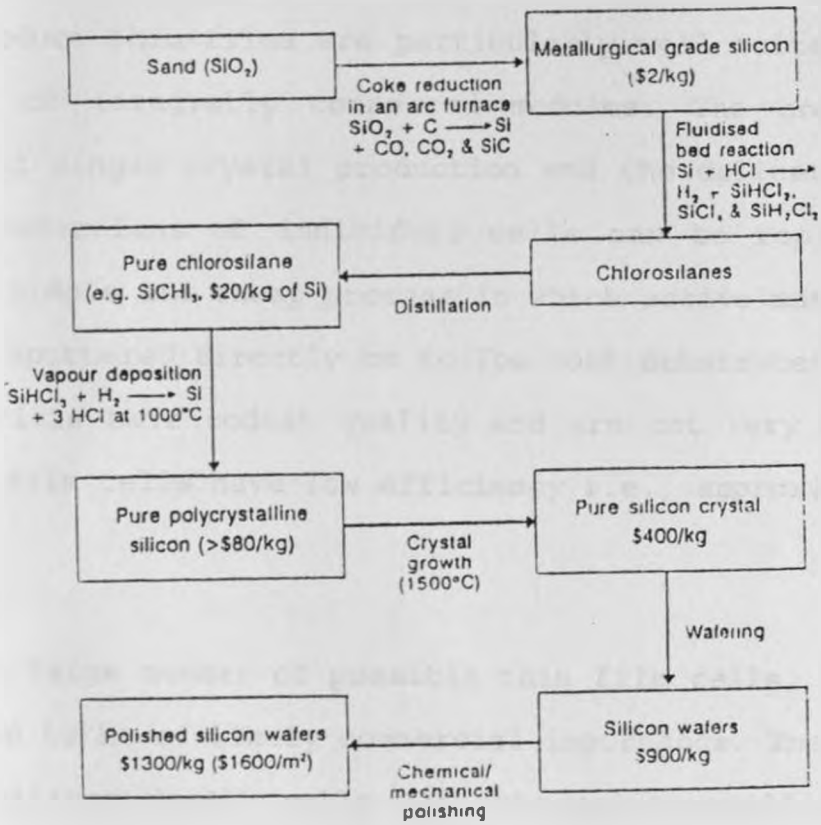


Fig. 1.4 Different steps in silicon production from sand [3]

Meanwhile, thin film based solar cells are also being investigated. It is believed that these cells can achieve lower costs than crystalline devices for two primary reasons. First, they absorb sunlight extremely well and lower quality material can be used without sacrificing much in the performance of the cells. Hence, only very thin active layer is required; about 1-10 μm as compared to 100 μm or so for crystalline cells [5]. Second, the techniques used to produce thin films are particularly well suited for mass production of integrally connected modules. The costly batch processes of single crystal production and the delicate handling and interconnections of individual cells can be replaced by a relatively simple and cheap process in which active materials are sprayed or sputtered directly on to low cost substrates. However, these materials have modest quality and are not very stable and hence thin film cells have low efficiency i.e., approximately 10% [4].

Amongst the large number of possible thin film cells, four types have emerged to be of likely commercial importance. These are the amorphous silicon (a-Si) cells [3], the polycrystalline silicon thin film cells [4], the copper indium diselenide/cadmium sulphide ($\text{CuInSe}_2/\text{CdS}$) heterojunction cells and, the cadmium telluride/cadmium sulphide (CdTe/CdS) heterojunction cells [5].

However, before thin film devices can become competitive with silicon solar cells, several problems must to be solved. The major

ones are the degradation and stability problems created by chemical reactions and modifications of thin films during operation under changing humidity, temperature and illumination. The major research and development effort has been to control the physical and chemical properties of thin film materials and to increase the efficiency and the reproducibility of the devices.

A third possibility which is being looked into is the application of thin film techniques coupled with liquid media to form a solid-liquid junction. In fact, the first photovoltaic device was a solid-liquid based cell constructed by Becquerel in 1839 [1]. In the next section we will compare photovoltaic energy conversion in solid state and semiconductor-electrolyte junctions.

1.3.3. Solid State Solar Cells.

In general, a solar cell operation is based on the ability of semiconductors to convert sunlight into electricity. The photons absorbed from the incident light create electron-hole pairs in the semiconductor. These pairs are separated by the device structure and transformed into electric current across the device.

The photogenerated carriers can be separated if an electrostatic field pulling electrons and holes in opposite directions exist. Such field is built in the structure of the cell by forming a junction between two different regions.

In a solid state junction, the field is created by a space charge region adjacent to the junction and resulting from the diffusion of the majority carriers across the contact. At equilibrium, this region is practically depleted of mobile charge carriers and the electric field prevents further diffusion of electrons and holes. Figure 1.5 illustrates the situation on a p-n junction. The solid state junction may be an interface between the n and p regions of one semiconductor (p-n junction), between two different semiconductors (heterojunction) or between a metal and a semiconductor (Schottky barrier). To widen the transition zone, a layer of intrinsic material is sometimes incorporated between the n- and p-type regions. In general, the formation of solid junctions requires sophisticated and expensive technology. Nevertheless, thin film solar cell offers the hope of inexpensive technology.

1.3.4 Solid Semiconductors-electrolyte based Cells (Wet Cells).

a. Advantages and Types of Wet Junction

Liquid junctions have received growing attention because of their potential for ultimately producing economical electricity and alternative fuels - such as hydrogen - from solar energy [6]. Such a junction is made by simply dipping the semiconductor in the electrolyte after forming an ohmic contact on one of its faces and insulating this face from the electrolyte. In contrast to the solid state device, no elaborate techniques are required to insure good junction.

The contact between a liquid and a solid can be more uniform and intimate compared to the contact between two solids. Thus, the effects of lattice mismatch and thermal expansion are minimized and, both single crystals and polycrystalline materials can be used as photoelectrode [7,8]. A better control of contact barrier heights in a wet cell is also possible since redox potentials in solution can be easily controlled in comparison to work function or electron affinity in semiconductors [8].

However, the biggest advantage of liquid junction devices compared to solid state devices is their capability to store energy [9,15]. In fact, photoelectrochemical conversion can be combined with electrochemical storage if suitable redox couples are used in the solution. Thus, an auxiliary storage system needed for solid state devices is not required. Figure 1.6 shows (a) the storage current, (b) the photocurrent and, (c) the output current on two days operation of an n-Cd(Se,Te)/aqueous $\text{Cs}_2\text{S}_x/\text{SnS}$ PEC cell. It can be observed, from Fig. 1.6, that the output current is near constant i.e., insensitive to light variation and the overall solar to electrical conversion efficiency is approximated to 11.3%.

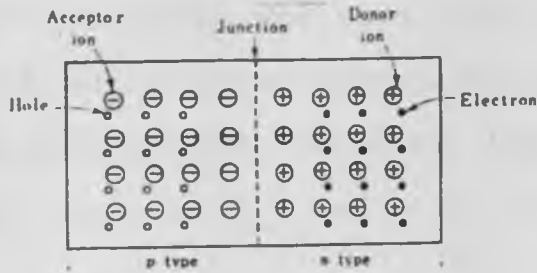


Fig.1.5. Contact barrier potential at a solid state junction.

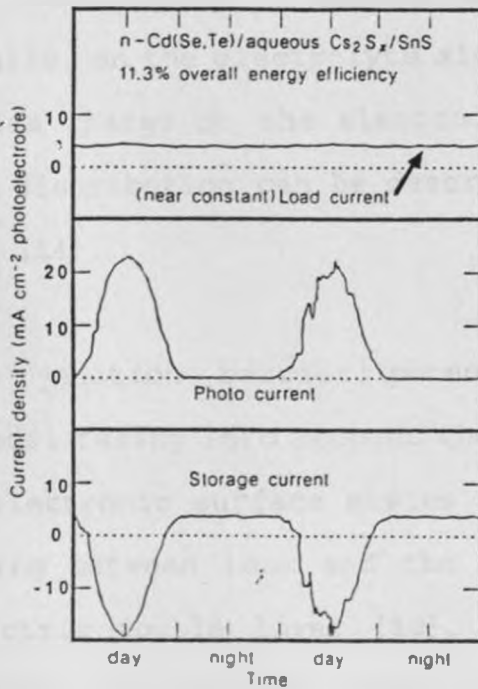


Fig. 1.6. Two days operation of an n-Cd (Se,Te)/aqueous $\text{Cs}_2\text{S}_x/\text{SnS}$ PEC cell with in-situ storage [9].

At present, three types of electrolyte/semiconductor junction are being studied; namely photoelectrolytic, photogalvanic and photoelectrochemical cells. In the former, solar energy is converted into chemical energy and then into electrical energy [7,10,11]. The second and the third convert sunlight directly into electricity, but in photogalvanic cells the light is absorbed in the solution [7,12] while in PEC cells it is absorbed in the semiconductor.

b. Junction Barrier Formation

In general, when any two phases are in contact, charge carriers diffuse across the interface until equilibrium is reached. In case of a semiconductor-electrolyte interface, the process creates a space charge (depletion) layer - needed for the charge separation mechanism during illumination - underneath the semiconductor surface [8]. Meanwhile, on the electrolyte side ions are rearranged such that the excess charge on the electrode surface is exactly balanced. The ions distribution can be described by the Helmholtz double layer model [14].

The corresponding junction barrier potential can better be represented by a model taking into account the space charge region, the existence of electronic surface states on the semiconductor, the chemical bonding between ions and the semiconductor surface atoms and the electric double layer [10]. Figure 1.7 shows the electric double layer, the spatial charge q and potential ϕ

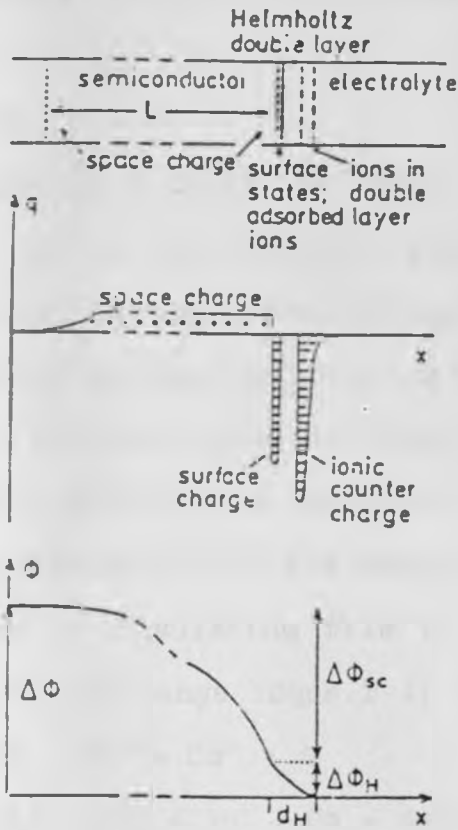


Fig. 1.7. The electric double layer and, the distribution of spatial charge q and potential at an n-type semiconductor-electrolyte interface.

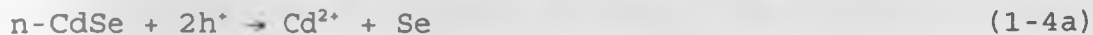
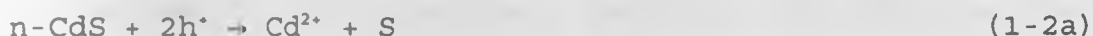
distributions at an n-type semiconductor-electrolyte interface. The total potential drop $\Delta\phi$ across the interface is

$$\Delta\phi = \Delta\phi_{sc} + \Delta\phi_H \quad (1-1)$$

where $\Delta\phi_{sc}$ is the potential drop across the depletion layer and $\Delta\phi_H$ is the potential drop in the Helmholtz double layer [14].

c. Stability

The formation of a depletion layer is a necessary condition for photoeffect at a semiconductor-electrolyte interface. But, the presence of photogenerated electrons or holes at the surface causes bonds weakening between neighboring atoms. The surface atoms become susceptible to react with the ionic species of the solution and undergo ionic oxidation or reduction. These corrosion reactions may lead to the dissolution of the semiconductor (Eqns.1-2) [7], to the formation of an insulating film on the photoelectrode (Eqn.1-3) [11] or to ion exchange (Eqns.1-4) [11].



The process involves holes as reactants in case of oxidation and electrons in case of reduction and is responsible for the instability and lower efficiency of wet cells. All surface atoms are statistically involved in the corrosion process, but the ones at some particular surface sites such as lattice imperfections are chief candidates. The importance of the phenomenon varies for each semiconductor with the particular electrolyte. All presently known semiconductors are susceptible to photodecomposition. But whether or not it occurs really depends to a large extent on kinetics. The semiconductor decomposition can be slowed or prevented by creating competitive redox reactions and stabilizing local structural defects on the surface.

d. Efficiency

The structure sketched in Fig. 1.8 has been suggested for a PEC solar cell [8,10,13]. The electrolyte is sandwiched between two electrodes and only a very thin layer < 1.0 mm is needed for creating the semiconductor surface barrier. It contains two species, one electrochemically reducible and the other oxidable. The working electrode is a semiconductor consisting of a thin film on a suitable substrate with ohmic contact. The counterelectrode can be a thin grid metal deposited on glass which will serve as a cover.

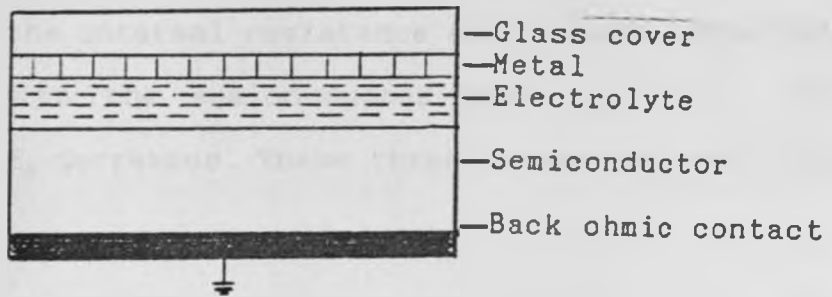


Fig. 1.8. Possible structure of a PEC cell.

As for solid state devices, a wet device parameters are the open circuit voltage V_{oc} , the short circuit current I_{sc} and the fill factor ff . The device efficiency is given by [3]:

$$\eta = \frac{V_{oc} \times I_{sc} \times ff}{W_{sun}} \quad \text{with} \quad ff = \frac{V_{max} \times I_{max}}{V_{oc} \times I_{sc}} \quad (1-5)$$

where V_{max} and I_{max} are the photovoltage and the photocurrent at the point where their product reaches a maximum, W_{sun} is the solar irradiance. The fill factor is controlled by the processes of recombination, the internal resistance and the electrode kinetics. V_{oc} increases with the semiconductor band gap E_g while I_{sc} increases when E_g decreases. These three parameters are related by [3,10]:

$$V_{oc} = \frac{kT}{q} \ln \left(\frac{I_{sc}}{I_o} + 1 \right) - \text{loss factor} \times \frac{E_g}{q}$$

where I_o is the dark saturation current. The fundamental maximum value E_g/q can be approached but not reached i.e. $V_{oc} < E_g/q$ due to losses. Losses are due to fundamental or technological limitations such as incomplete absorption of light, reflection, incomplete collection of carriers (recombination), etc. [3,11,16].

The optimum band gap ~ 1.3 eV for a theoretical maximum efficiency of 30% is deduced. For E_g in the range 1.1 eV to 1.7 eV, η exceeds 20%. Large band gap materials such as TiO_2 , CdS, etc are poor

sunlight converters. However, intensive efforts are being made to increase their photon harvesting capability [13,17-20].

In the section above we have highlighted that the major problems associated with wet solar cells are the chemical instability of the semiconducting electrodes, the conversion efficiency and the cell cost. Solution to these problems require development of stable systems with satisfactory optical and electrical properties. This is to say that material problems are yet to be solved before wet cells can become commercially successful.

1.4 Materials for Wet Solar Cells.

The application of semiconductor to the construction of photoelectrochemical photovoltaic and photoelectrolytic cells has been reviewed by Nozik [21]. The investigations of such electrodes are concerned with the fundamental studies of the semiconductor/electrolyte interface and the construction of efficient systems for electrical power generation or chemical species production from sunlight. However, the practical application of such devices depends on the discovery of inexpensive materials with energy gap which matches the solar spectrum and which are capable of stable operation in solution over an extended period. This has led to the investigation of a number of new materials.

According Tributsch [15], the most promising electrode materials are transition metal dichalcogenides. These compounds have formula MX_2 , where M is the transition metal atom and X is one of the chalcogens S, Se or Te. They are about 60 in number and can roughly be divided into two classes: layered compounds and pyrite type compounds [22].

A large variety of semiconducting transition metal dichalcogenides have been prepared using various techniques. The techniques include high pressure synthesis [23,24], thermal evaporation [25], and chemical vapor transport; among others. Physical and chemical properties of interest for solar energy application have been investigated in natural crystals as well as in synthetic ones. The physical properties include structural, electrical, optical and magnetic properties.

The most studied transition metal dichalcogenides are the layered compound semiconductors [26-31]. They show reasonable efficiency and good stability in relatively oxidizing solutions. In general, the compounds exhibiting semiconducting properties are those formed from the groups IVB and VIB columns. The compounds MoS_2 , WS_2 , $MoSe_2$ and WSe_2 appear to have particularly desirable semiconducting properties [15].

Mattheiss [31] has proposed a band structure model for these layered compounds. Wrighton [26] studied MoS_2 based PEC solar cells

using non-aqueous solutions. A band gap $E_g = 1.75$ eV was estimated. The electrode showed interesting stability but low efficiency. The same authors reported high efficiency and good stability for MoSe_2 in acetonitrile solution containing Cl^-/Cl_2 [28]. Heller [11] described 10% efficient single crystal n- WSe_2 /Iodide-Triiodide/C system. Fu-Ren and co-workers [27] reported an efficiency of 14% for the same system using a Platinum counterelectrode and 11% when the previous redox couple is replaced by Bromide-Bromine. The latter redox couple gave lower fill factor and open circuit voltage but high short circuit current due to lower absorbance of Br^-/Br . These authors also considered the rechargeable p- WSe_2 /MV $^{2+}$ -I $^-$ /n- WSe_2 system; MV being methylviologen. The system n- WSe_2 /MV $^{2+}$ -I $^-$ /p- WSe_2 generated hydrogen. All these system show good stability and reasonable efficiencies.

The second subclass of transition metal dichalcogenides - pyrite type compounds - have also attracted a lot of interest the last two decades. Pyrite itself has received growing attention as a useful material for solar energy application [32-35]. It has been considered as a depolarizer anode for hydrogen production and a cathode in high-energy-density batteries [1]. Natural and synthetic pyrite has been widely studied [24,32-41]. From these earlier studies it is a confirmed fact that pyrite FeS_2 is a semiconducting material.

Various authors have analyzed electrical data of iron pyrite [24,38,41]. In those studies the reported values of the Hall mobility, the resistivity (activation energy) and the Seebeck voltage are found to vary over a wide range and both p- and n-type conduction are reported. This can be explained by variation in impurity concentration in different samples.

Optical data of FeS_2 have also been intensively analyzed. Sato [35] and Bither [24] analysed the reflectivity spectrum of pyrite FeS_2 with the help of Kramers-Kronig transformation from which the optical constants were calculated. Schelgel [39] and Kou [40] reported on optical absorption in iron pyrite.

By virtue of its constituent elements and the material's properties, pyrite FeS_2 has seemed to be a recent candidate for PEC cells [43]. Iron is the second most abundant metal after aluminum and fourth most abundant element in the earth's crust [45]. The sulfur occurs widely as element in free state and is an important constituent of petroleum - gaseous fuels H_2S and S_2O . It is also available in innumerable sulfide ores of metals and in various sulfates [36].

As we shall see in section 2.3, Iron pyrite has the advantage of being a d-transition material [37] in which the photogeneration of carriers involves non-bonding orbitals i.e $d(t_{2g}) \rightarrow d(e_g)$ electronic transition. Thus, bond breaking is avoided [15,34]. These lead to

the ability of the material to be used in a wet cell without photo-corrosion [15,22,27]. Its narrow indirect band gap of 0.9-1.2 eV and high absorption coefficient $\sim 10^5 \text{ cm}^{-1}$ [44]; its relatively long diffusion length $L > 0.12\text{-}1.0 \mu\text{m}$ [43] and high Hall mobility $\mu > 230 \text{ cm}^2\text{V}^{-1}\text{s}^{-1}$ [24] are other properties suggesting iron pyrite as a promising photoelectrochemical material.

So far the investigations have mostly been concerned with natural or synthetic crystals of this material. But, due to the many difficulties found in growing large area synthetic pieces needed for solar energy application, attempts are being made to obtain semiconducting FeS_2 thin films. Different techniques have been used: thermal evaporation [25], sulfidation of iron [42] or iron oxides films [43], vapor phase epitaxial growth [44], etc. However, it has been observed that synthetic crystals or thin films do not represent the properties of pure pyrite due to the presence of trace amounts of conductive metallic FeS or deviation from the ideal stoichiometry. This deviation occurs as sulfur deficiency which introduces intermediate states in the mid band gap decreasing the barrier height at the FeS_2 /electrolyte junction [43]. Karguppikar [25] found a S/Fe ratio equal to 1.4 in pyrite FeS_2 films prepared by thermal evaporation. Ferrer [42] reported value of 1.8 for films prepared by sulfidation of iron films and, Smestad [43] obtained films nearly 100% pyrite by sulfidation of iron oxide films. Sulfur treatment seems to improve the purity of the material.

Crystalline and thin film FeS_2 have been considered by Tributsch et al as photoelectrode in wet cells [32-34,43,44]. Among various electrolytes studied, the most favorable was found to be aqueous I^-/I^{3-} redox system which gave a quantum efficiency close to 100% and stabilized n- FeS_2 electrode to 100% [33]. However, it was observed that the surface and trapping states arising from deviation from the ideal stoichiometry affected the cells performance drastically. In fact, these states interact with the redox system, and hence, reduce the photocurrents and voltages [34,43].

Despite the above advantages and breakthrough, the material shows a poor photoresponse - i.e. low photocurrents and voltages - in current PEC configurations and need to be further investigated. More research is needed to improve the materials stoichiometry and purity, its bulk and interfacial properties and to understand its solid state chemistry, and hence, to increase its photoactivity.

1.5 Objectives.

Some work - concerned with solid state solar devices - has been carried out in Physics laboratory at the University of Nairobi. Ceramic CdS/CuS [46], crystalline silicon [47] and some transparent conducting thin films [48-51] have been investigated. This work intend to open way to research on materials useful for wet solar cells. It is aimed to grow pyrite FeS_2 thin films by spray pyrolysis followed by sulfur treatment. The deposition parameters will be identified and optimized. The crystallographic, optical and electrical properties of the films will be investigated.

CHAPTER TWO

THEORETICAL BACKGROUND.

2.1. Iron Pyrite Crystal.

Iron pyrite FeS_2 crystallizes in isometric system and has four formula units per unit cell [36]. Each metal atom is surrounded by six nearest-neighbor anions in a distorted octahedral environment, while each anion bonds to one anions and three cations in a distorted tetrahedral arrangement. In the resulting structure, Fe atoms are situated at the face centers and corners of a cube. Meanwhile S atoms appear in dumbbell pairs centered at the midpoints of the cube edges and at the cubes body center. The dumbbell are ordered equally along the four $\langle 111 \rangle$ directions of the cube i.e. parallel to the body diagonal directions. This structure is illustrated in Fig. 2.1.

2.2. Band Structure of Solids.

According to the quantum theory, the electrons of a single free atom have well defined discrete energy levels. When atoms are brought into close proximity to form a crystal, their energy levels split into energy bands as a result of the coupling between their outer-shell electrons. The bands are made of closely spaced energy levels instead of the widely separated levels of isolated atoms.

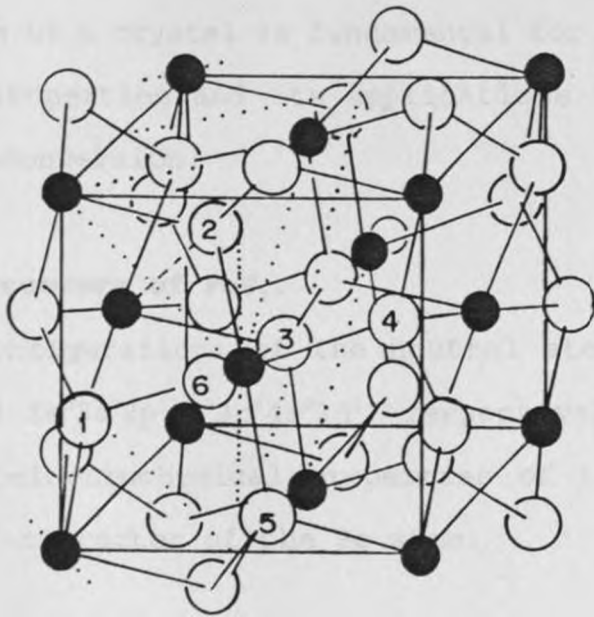


Fig. 2.1 Crystal structure of iron pyrite (● : Fe and ○ : S) [22]

The energy bands are separated by forbidden gaps i.e. energy regions in which no allowed states can exist and can be grouped into valence bands and conduction bands. The valence region is made of filled bands while vacant and half filled bands constitute the conduction bands; see Fig.(2,10) and (2,11). The energy of the top of the valence band is denoted by E_v and the energy of the bottom of the conduction band is denoted by E_c . The difference between the two band edges is called the energy gap E_g :

$$E_g = E_c - E_v \quad (2-1)$$

The band structure of a crystal is fundamental for an understanding of its physical properties and its applications in electronic or for solar energy conversion.

2.3 Electronic Structure of FeS_2 .

The electronic configurations of the neutral atoms S and Fe are $1s^2 2s^2 2p^6 3s^2 3p^4$ and $1s^2 2s^2 2p^6 3s^2 3p^6 4s^2 3d^6$, respectively. The semiconducting and photoelectrochemical properties of the compound FeS_2 arises from the d-character of the Fe atom.

When sulfur and iron atoms are brought together to form the pyrite FeS_2 , the orbitals of individual atoms mix to form the molecular bonding and antibonding bands as described by Wilson [22], Bither [34], Schelegel [39] and Bulet [37]. From the magnetic measurement, the metal cations in FeS_2 are believed to be divalent; thus the chalcogen pairs can also be viewed as divalent anions $(X_2)^{2-}$.

Figure 2.2 shows the schematic representation of the band limits as function of energy; the zero level corresponding to the highest occupied state.

Discrete bands can be observed on Fig.2.2. The two first bands lying at the strong binding energies arise from bonding and antibonding s-states between the sulfur S_2 pairs. The 3rd band is made of sulfur p-states and contains contribution from metal d-states. Next is the d-band i.e. a band overwhelmingly made of metal d-states. It is split into two sub-bands by the crystal electrostatic field. The first sub-band is completely filled with six electrons while the second one is empty. The semiconducting properties of the compound arise from the gap between these two sub-bands i.e. from $d(t_{2g}) \rightarrow d(e_g)$ electronic transitions. The antibonding S_2 $p\sigma^*$ band merges in the e_g sub-band although the p orbitals contribute principally at the top of this first conduction band. The second conduction band is made of the metal sp orbitals and has contribution from unoccupied sulfur p-orbitals.

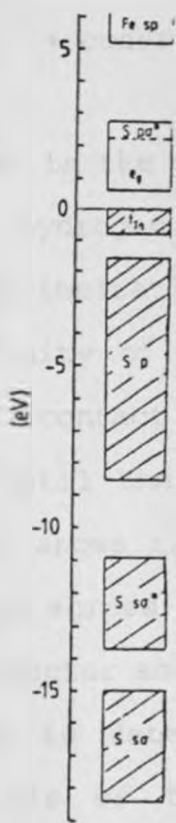


Fig. 2.2. Schematic representation of the band limits as a function of energy in pyrite FeS₂, [37].

2.4 Photoelectrochemical Mechanism.

The hypothetical situation before the electrolyte comes into contact with the electrodes is illustrated on Fig. 2.3. where ϕ and E_F are the work function and the Fermi level, respectively and the initials S, E(L), M designate semi-conductor, electrolyte(liquid) and metal. χ_s is the semiconductor electron affinity and $q\phi_n$ is the difference between the conduction band edge and the Fermi level. The electrolyte (redox) Fermi level E_{FL} is defined by [10]:

$$E_{FL} = -qV_{redox} + const \quad . \quad (2-2)$$

where the constant is the work function of a reference electrode; e.g., the normal hydrogen electrode. The redox potential V_{redox} is the average of the ionization energy of the reduced species and of the electron affinity of the oxidized species in the solution. After the physical contact is made, charge transfer occurs through both interfaces until the three Fermi levels line up with each other. Figure 2.4 shows the resulting semiconductor band-bending and potential drop across the interfaces. The band bend upward in an n-type semiconductor and downward in a p-type. The extending of the band bending is determined by the difference between the chemical potentials of the electrons in the solution (redox potential) and in the semiconductor (Fermi level). This difference represents the upper limit that the photovoltage can reach. For efficient PEC cell operation, the potential drop across the metal/electrolyte interface should be minimum i.e. $\phi_E \approx \phi_M$; this will be assumed. From Eqn. (1-1) and Fig. 2.4, the surface potential on the

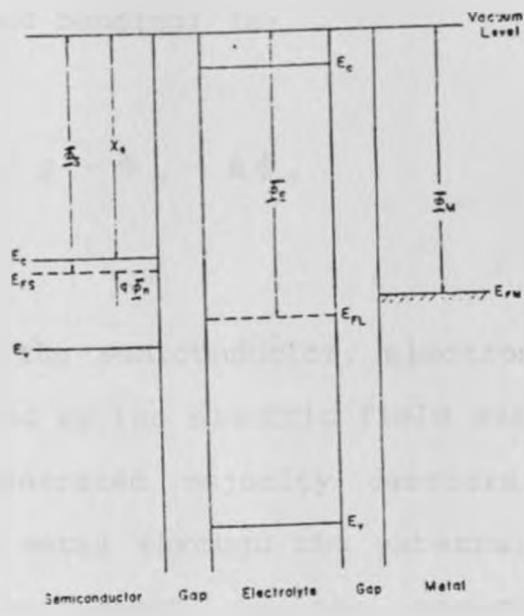


Fig. 2.3. Energy band diagram of an n-type semiconductor-electrolyte/metal system before physical contact and equilibrium.

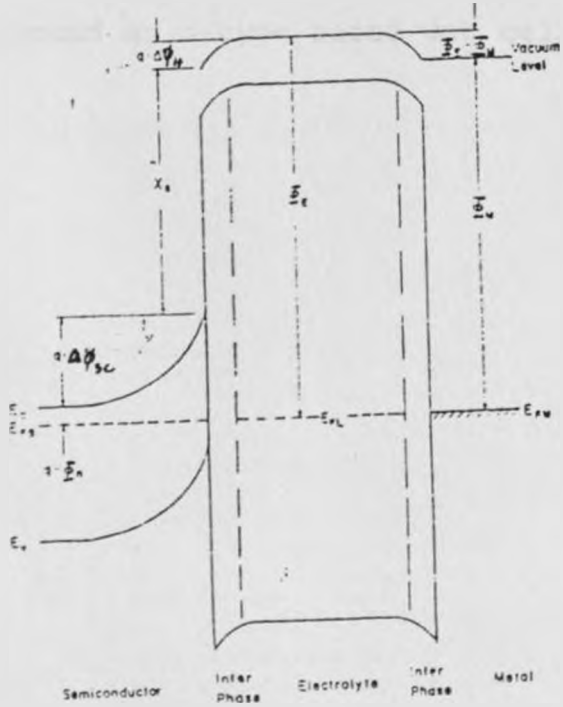


Fig. 2.4. Energy band diagram of n-type semiconductor-electrolyte/metal system after physical contact at equilibrium and zero bias and, in dark.

semiconductor (the band bending) is:

$$\Delta\phi_{sc} = (\Phi_E - \chi_s) / q - \Phi_n - \Delta\phi_H \quad (2-3)$$

Upon illumination of the semiconductor, electron-hole pairs are generated and separated by the electric field associated with the band-bending. Photogenerated majority carriers move from the semiconductor to the metal through the external load while the minority carriers are swept to the semiconductor-solution interface. Figure 2.5 show (a) the components of wet cells and the photoelectrochemical processes (b) in photoanode and (c) in photocathode based cells. It can be seen that holes oxidize the redox couple while electrons reduce it. Figure 2.6 shows the flow of charge carriers around an n-type based wet cell in series with a load.

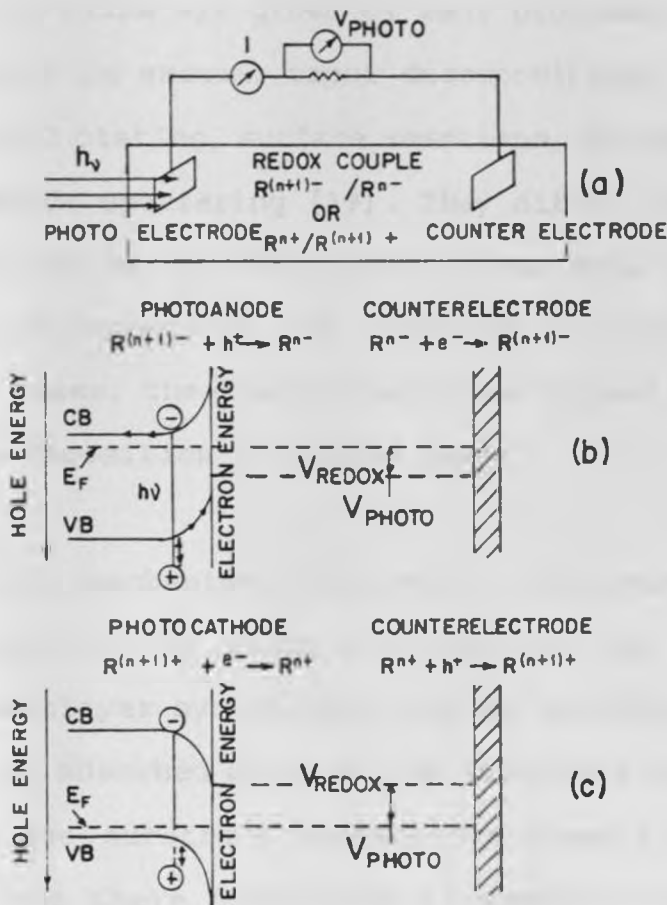


Fig. 2.5 Energy band diagram of a wet cell under illumination.

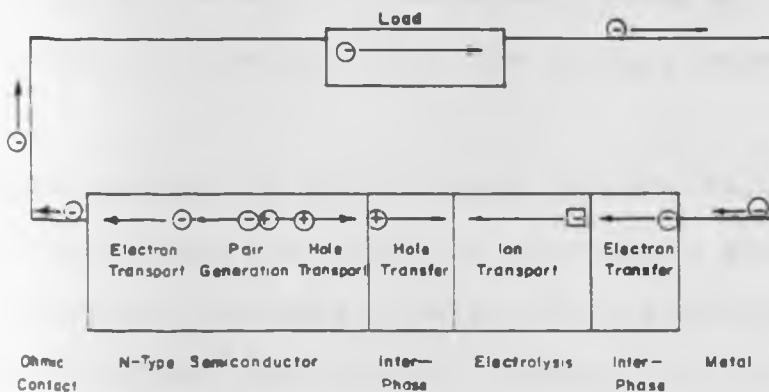


Fig. 2.6. Flow of charge carriers around a circuit of a PEC solar cell in series with a load.

2.5 Thin Films Growth.

Currently thin films are grown by many processes. The most common are evaporation in vacuum, vapor decomposition, chemical plating, electrochemical plating, surface reactions, cathode sputtering, and reactive cathode sputtering [39]. They differ in many fundamental aspects but can be grouped under three main methods: chemical attack, electrodeposition and condensation from the vapor phase [52]. In all cases, the growth conditions depend on the environment in which the deposition is taking place.

The fundamental mechanisms involved in the growth process at the earlier stages of the films formation is the same. The growth occurs not monolayer by monolayer but by the formation of discrete nuclei made of adsorbed atoms at the substrate surface [53]. Atoms arriving on the substrate surface are free to move and have a finite lifetime there before the re-evaporation. If during this time it can find a site to stick in, that site will act as a nucleus for further deposition and hence, larger aggregates are formed. These aggregates grow laterally and normal to the substrate surface by the receipt of new deposit atoms and by the receipt from the neighboring nuclei. Thus, the surface layer is formed.

The early stages of this process involve films that are discontinuous and made of a network of irregularly shaped nuclei [53]. As the thickness increases, the faults are eliminated and the film becomes coherent and uniform. However, the process is likely to

introduce lattice imperfections in the film.

The binding energy of an atom at the surface varies with the site to which it is held and with the nature of the cohesive forces. These forces have mainly two origins: van der Waals interactions between atoms and the substrate and, interactions of chemical natures i.e arising from the rearrangement of the electronic structure of the interacting entities. These interactions can be described in terms of a potential which is attractive at longer distances and repulsive at shorter distances. The attractive part is due to instantaneous dipole and quadripole moments of the surface atoms or molecules while the repulsion at shorter distances originates from the electron clouds [54]. The attractive component gives an energy proportional to $-1/r^6$ while the repulsive force is proportional to $e^{-r/a}$ [55]. This potential - known as Lennard-Jones potential - is illustrated in Fig. 2.7.

An atom held at the surface will be in a potential well and its mean lifetime in the well is given by [54]:

$$\tau = \tau_0 \exp \left(- \frac{\phi}{kT} \right) \quad (2-4)$$

The potential energy ϕ at the substrate surface plane can be represented by two terms ϕ_d and ϕ_e so that

$$\phi = \phi_d + \phi_e$$

where ϕ_d is the diffusion energy and ϕ_e , the re-evaporation energy.

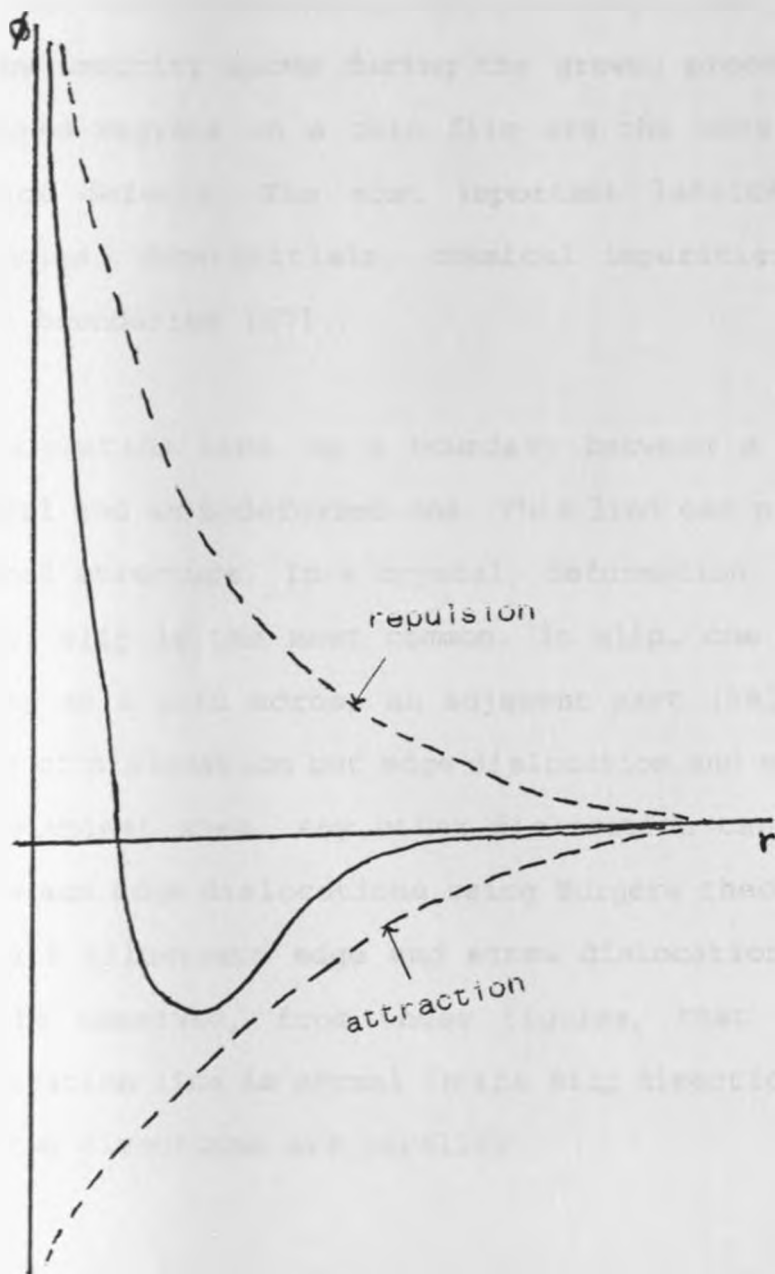


Fig. 2.7. Potential of interaction between the substrate and the striking atom.

2.6 Stresses and Defects in Thin Films

Thin film can be in a state of high mechanical stress originating from the difference in the thermal expansion coefficients of the substrate and the film material. In addition, intrinsic stresses [40] can be introduced by the freezing-in of the lattice defects and by impurity atoms during the growth process [54]. The highly strained regions in a thin film are the ones in the vicinity of lattice defects. The most important lattice imperfections are vacancies, interstitials, chemical impurities, dislocations and grain boundaries [57].

A dislocation line is a boundary between a deformed part of a crystal and an undeformed one. This line can propagate through the crystal structure. In a crystal, deformation can occur by various modes; slip is the most common. In slip, one part of the crystal slides as a unit across an adjacent part [58]. There are several types of dislocation but edge dislocation and screw dislocation are the simplest ones. Any other dislocation can be decomposed into screw and edge dislocations using Burgers theory [58]. Figures 2.8 and 2.9 illustrate edge and screw dislocations, respectively. It can be observed, from these figures, that in the former, the dislocation line is normal to the slip direction while in the later the two directions are parallel.

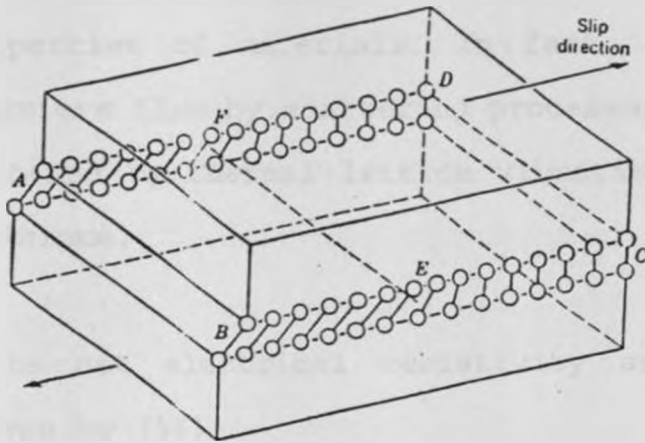


Fig. 2.8. An edge dislocation EF; ABEF is the slipped region while FECD is unslipped. The dislocation line extends indefinitely in the slip plan in a direction normal to the slip direction.

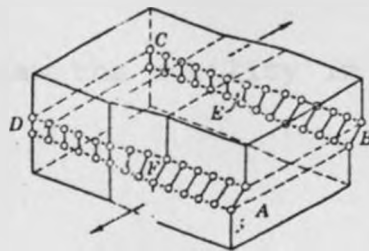


Fig. 2.9. A screw dislocation Ef with ABEF the slipped region and FECD unslipped. The dislocation line is in the slip direction.

2.7 Charge Carriers Scattering.

The lattice imperfections play a vital role in the electrical transport properties of materials. In fact, the imperfections reduce the carriers flow by scattering processes. Charge carriers are also scattered by thermal lattice vibration i.e. by phonon-electron collisions.

In metals, the net electrical resistivity arising from these effects is given by [55]:

$$\rho = \rho_L + \rho_i \quad (2-5)$$

where ρ_L is the resistivity caused by phonon-electron collisions, and ρ_i is due to impurities and lattice defects scattering. The former term is temperature dependent and the later is not. This empirical relation expresses Mathiessen's rule and hold if the two sources of scattering are independent of one another. The lattice resistivity ρ_L is the same for different specimens of a metal, even though ρ_i may vary widely. It vanishes as $T \rightarrow 0$ such that at absolute zero, the residual resistivity is $\rho(0) = \rho_i$

From Mathiessen's law the mobility in a semiconductor should be written [59]:

$$\frac{1}{\mu} = \frac{1}{\mu_L} + \frac{1}{\mu_i} \quad (2-6)$$

But, this is rather inaccurate. Nevertheless, it presents a mean of understanding the typical mobility curves of semiconductors. The inaccuracy results from two main differences between metals and semiconductors. First, in metals, charge carriers are electrons with higher concentrations while in semiconductors, carriers concentrations are relatively low and account has to be taken of holes in the valence band. Second, the scattering process in a semiconductor is more complex because it depends markedly on changes in the actual total carriers densities, through doping, optical excitation, diffusion, trapping, etc.

2.8 Direct and Indirect Transitions.

Semiconductor crystals have complex band structures as illustrated in Fig. 2.10 for Germanium, Silicon and Gallium Arsenic. But the parabolic simplifications as in Fig. 2.11 can be used to describe the general features.

A semiconductor is a direct band gap material if the lowest point of the conduction band, occurs at the same value of k as the highest point of the valence band as indicated on Figs. 2.10(c) and 2.11(a). Thus, a direct optical transition takes place with no significant change in k because the absorbed photon has a very small wavevector. In the process, a photon is absorbed with creation of an electron-hole pair. The threshold frequency ω_g for absorption by direct transition determines the direct energy gap:

$$E_g = \hbar\omega_g \quad (2-7)$$

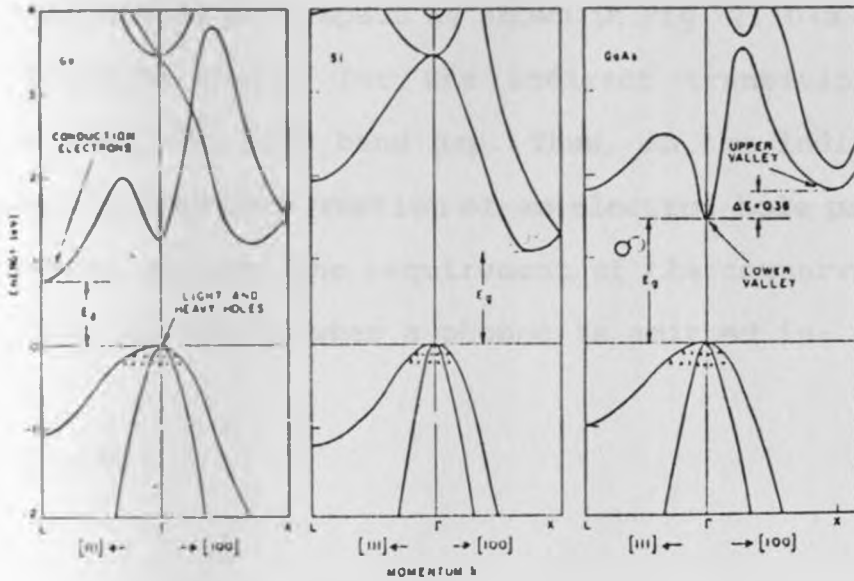


Fig. 2.10 Energy band structures of Ge, Si, and GaAs. (+) and (-) indicate holes and electrons, respectively [43].

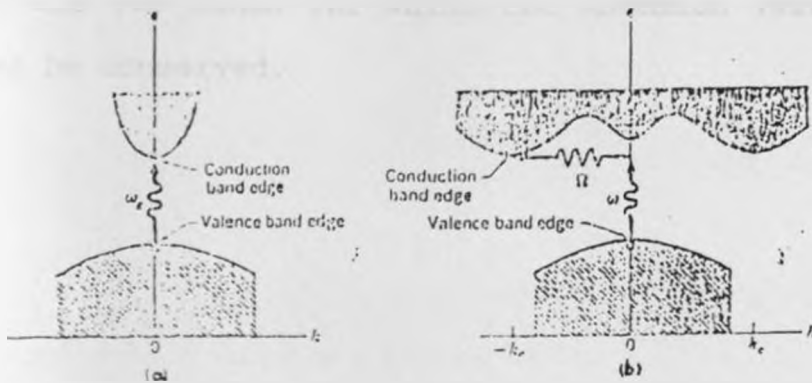


Fig. 2.11 Energy-crystal momentum relationship. (a) direct and (b) indirect transitions.

An indirect band gap semiconductor is the one in which, the conduction and valence bands edges are not aligned but they are widely separated in k-space as shown in Fig. 2.10(a-b) and 2.11(b). The threshold energy for the indirect transition is therefore greater than the true band gap. Thus, in the indirect absorption process, further the creation of an electron-hole pair, a phonon is involved to satisfy the requirement of the conservation laws. The absorption threshold when a phonon is emitted is:

$$\hbar\omega = E_g + \hbar\Omega \quad (2-8)$$

where Ω is the frequency of the phonon of wavevector $\vec{K} = -\vec{k}_c$. At higher temperatures phonons are already present and if a phonon is absorbed along with a photon, the threshold energy is:

$$\hbar\omega = E_g - \hbar\Omega \quad (2-9)$$

In the above discussion only the threshold transitions are considered while transitions occur generally between almost all points of the two bands for which the momentum (wavevector) and energy can be conserved.

2.9. Absorption Coefficient.

The ability of a semiconductor to absorb the light of a given wavelength is given by the absorption coefficient $\alpha(\lambda)$. The incident light inside a semiconductor falls off in intensity by $1/e$ for each $1/\alpha$ distance. Thus the absorption coefficient determines the thickness of the semiconductor used for complete absorption of light. Only incident photons of energy $h\nu \geq E_g$ can be absorbed while for $h\nu < E_g$, the semiconductor is transparent ($\alpha=0$).

Near the absorption edge, the band to band transition probability becomes constant [40]. Then the variation of the absorption coefficient with photon energy is of the form:

$$\alpha = \alpha_0 (h\nu - E_g)^n \quad (h\nu \geq E_g) \quad (2-10)$$

where $n=1/2$ for direct allowed transition, $n=3/2$ for direct forbidden transition, $n=2$ for indirect allowed transition, and $n=3$ for indirect forbidden transition [16,40].

This equation provides an important tool which can be used to estimate the energy gap of a semiconductor. In fact, for direct transition, we can write

$$\alpha = \alpha_0 (h\nu - E_g)^{1/2} \quad \text{or} \quad \alpha^2 \propto (h\nu - E_g) \quad (2-11)$$

A plot of α^2 or of $(\alpha h\nu)^2$ vs $h\nu$ should yield a straight line with the intercept on $h\nu$ axis corresponding to the energy gap.

similarly, for the indirect transitions, we have

$$\alpha = \alpha_0 (h\nu - E_g)^2 \quad (2-12)$$

and the indirect energy gap is obtained from the plot of $(\alpha h\nu)^{1/2}$ vs $h\nu$. A line with two gradients should be obtained in this case, the two intercepts on the energy axis corresponding to $E_g + E_p$ and $E_g - E_p$; E_p being the energy of the phonon involved in the process.

2.10. Transmission and Reflection

Free charge carriers in a semiconductor have a marked influence on the optical properties of the medium [60]. In general, the interaction of light with matter is described by Maxwell equations [61]. The optical characteristics of the medium is derived from these equations in term of complex parameters which describe the dispersive - real parts - and absorptive - imaginary parts - aspects of the process [61]. Two complex parameters which can be considered are the index of refraction

$$N = n + ik \quad (2-13)$$

and the dielectric constant

$$\epsilon = \epsilon_1 + \epsilon_2 \quad (2-14)$$

where n is the ordinary refractive index, k is the extinction coefficient and, ϵ_1 and ϵ_2 are the real and the imaginary dielectric constants. The optical constants (n,k) are related to the dielectric constants by [61]:

$$\epsilon_1 = n^2 - k^2 \quad \text{and} \quad \epsilon_2 = 2nk \quad (2-15)$$

The reflectivity R at any absorbing medium of indices (n,k) in air for normal incidence is given by [16]:

$$R = \frac{(1-n)^2 + k^2}{(1+n)^2 + k^2} \quad (2-16)$$

The transmission coefficient T and the reflection coefficient R for normal incidence are related by [16]:

$$T = \frac{(1-R^2) \exp(-\alpha t)}{1 - R^2 \exp(-2\alpha t)} \quad (2-17)$$

When αt is large i.e. around the absorption edge, the second term in the denominator can be neglected and the expression reduces to

$$T = (1-R^2) e^{-\alpha t} \quad (2-18)$$

or, if the reflection can also be neglected:

$$T = e^{-\alpha t} \quad (2-19)$$

2.11. Resistivity and Hall Effect.

The resistance R of an conductive film is related to its length l , width b and thickness t by [60]

$$R = \rho \frac{l}{bt} \quad (2-20)$$

where ρ is the resistivity of the film.

This equation can be written

$$R = R_s \frac{l}{b} \quad \text{where} \quad R_s = \frac{\rho}{t} \quad (2-21)$$

is the sheet resistance which can be measured by the two points probe method. The temperature variation of the resistance can be expressed by

$$R = R_0 \exp \left(-\frac{E_a}{kT} \right) \quad (2-22)$$

where E_a is the activation energy and k is the Boltzman constant. A plot of $\ln R$ vs $1/T$ should be a straight line and the slope of this line can give an estimation of the activation energy.

The conductivity σ is defined as: $\sigma = 1/\rho$

In terms of the carrier concentrations n (electrons) and p (holes) the conductivity can be written as [16]:

$$\sigma = \mu_n n e + \mu_p p e \quad (2-23)$$

where μ_n and μ_p are the electron and hole mobilities.

The carriers concentration and carriers type (electron or hole) in a semiconductor can be obtained using Hall effect. If a conductor (metal or semiconductor) carrying a current I is placed in a

transverse magnetic field B , an electric field E is induced in the direction perpendicular to both I and B ; this is the so called Hall effect. If in Fig. 2. 12 I is in the positive x direction and B in the positive z direction, charge carriers will be deflected - by the Lorentz force - in the negative y direction. This deflection causes carriers accumulation on one side resulting in a potential difference across the specimen; the so called Hall voltage under open circuit condition. Hence, an electric field is created in the negative (electrons) or the positive (holes) y direction to balance the deflection. Thus, the semiconductor will be n-type if the polarity of V_H is positive at terminal 2 with respect to terminal 1 and p-type if vice versa.

Under steady state conditions, we have

$$eE = evB \quad (2-24)$$

where e is the electric charge of each carrier, v is the drift velocity, and eE and evB are respectively the electric and magnetic forces on a charge carrier. The Hall voltage V_H and the electric field E are related by

$$E = V_H / b \quad (2-25)$$

where b is the width of the film. Assuming that the current I is made up of n free charge carriers per unit volume, we can write

$$I = nevbt \quad (2-26)$$

Using Eqns. (2-24) to (2-26), we get the Hall voltage

$$V_H = R_H \frac{IB}{t} \quad (2-27)$$

where κ_H is the Hall coefficient defined by

$$R_H = \frac{1}{n e} \quad (2-28)$$

In the above we have assumed that the conduction is due primarily to electrons ($n \gg p$); thus $\sigma = \mu_n n e$. It is also assumed that all the particles travel with the mean drift velocity i.e. the random thermal distribution in velocity is neglected. Under these conditions, the Hall mobility and the drift mobility are the same [16]. The carrier concentration n and the Hall mobility μ_H are therefore given by

$$n = \frac{1}{R_H e} \quad \text{and} \quad \mu_H = R_H \sigma \quad (2-29)$$

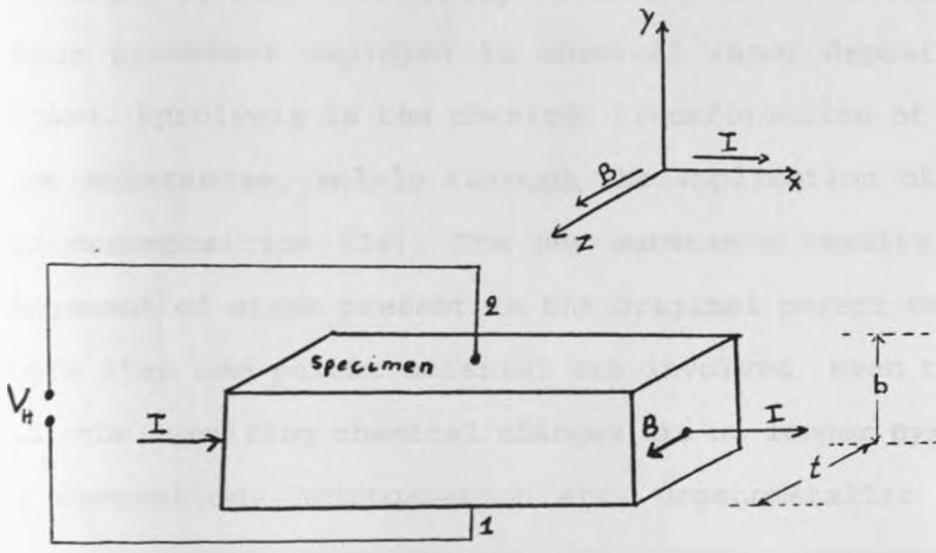


Fig. 2.12. Experimental set-up for Hall measurement.

CHAPTER THREE

EXPERIMENTAL TECHNIQUES.

3.1. Spray Pyrolysis.

The spray pyrolysis technique is a versatile method. It has been used successfully in glass works, metal coatings, semiconductor devices manufacturing etc. Both vitreous and crystalline films of element and compound materials have been prepared at relatively low temperatures.

The technique is based on pyrolytic decomposition which is one of the major processes employed in chemical vapor deposition (CVD) techniques. Pyrolysis is the chemical transformation of a material into new substances, solely through the application of heat i.e. thermal decomposition [36]. The new substance results only from rearrangement of atoms present in the original parent material. In case more than one parent material are involved, even though heat is used, the resulting chemical changes are no longer pyrolytic; it may be combustion, hydrogenation etc. Organometallic compounds, hydrides and metal hydrides are particularly suitable starting materials [52].

The spray pyrolysis is basically a material synthesis method. It involves spraying a solution containing soluble salts of the constituents atoms of the desired compound on a substrate. The substrate is maintained at elevated temperature such that the spray droplets reaching on it undergo thermal decomposition. The

constituents of the liquid phase react to form nuclei of the solid phase. The undesired by-products and the excess solvent escape in the vapor phase.

All sites of the substrate surface are statistically involved, but the distribution of nucleation sites depends on the characteristics of the surface. Those with strong bonds are particularly favorable nucleation sites [52]. The growing nuclei come in contact and coalesce to form a coherent film. This growth process is activated by the thermal energy from the substrate. Therefore, the substrate temperature and also its surface conditions are of fundamental importance in controlling the film properties. One of the challenges in preparing high quality films by this technique, is to minimize the high porosity and irregular texturing associated with volume shrinkage, and the evolution of gaseous by products.

3.2. Experimental set - up.

The experimental set-up is shown in Fig. 3.1. The sprayer, made of hard glass, has a single outlet but two inlets; one for the solution and the other for the carrier gas. To obtain a fine spray, the outlet is a fine capillary of dimensions $d = 1$ mm and $a = 2$ mm. Nitrogen was used as carrier gas.

The solution on reaching the outlet was sprayed by the carrier gas; the gas pressure was controlled by a flowmeter. This fine spray was directed on a glass substrate placed on a hot plate.

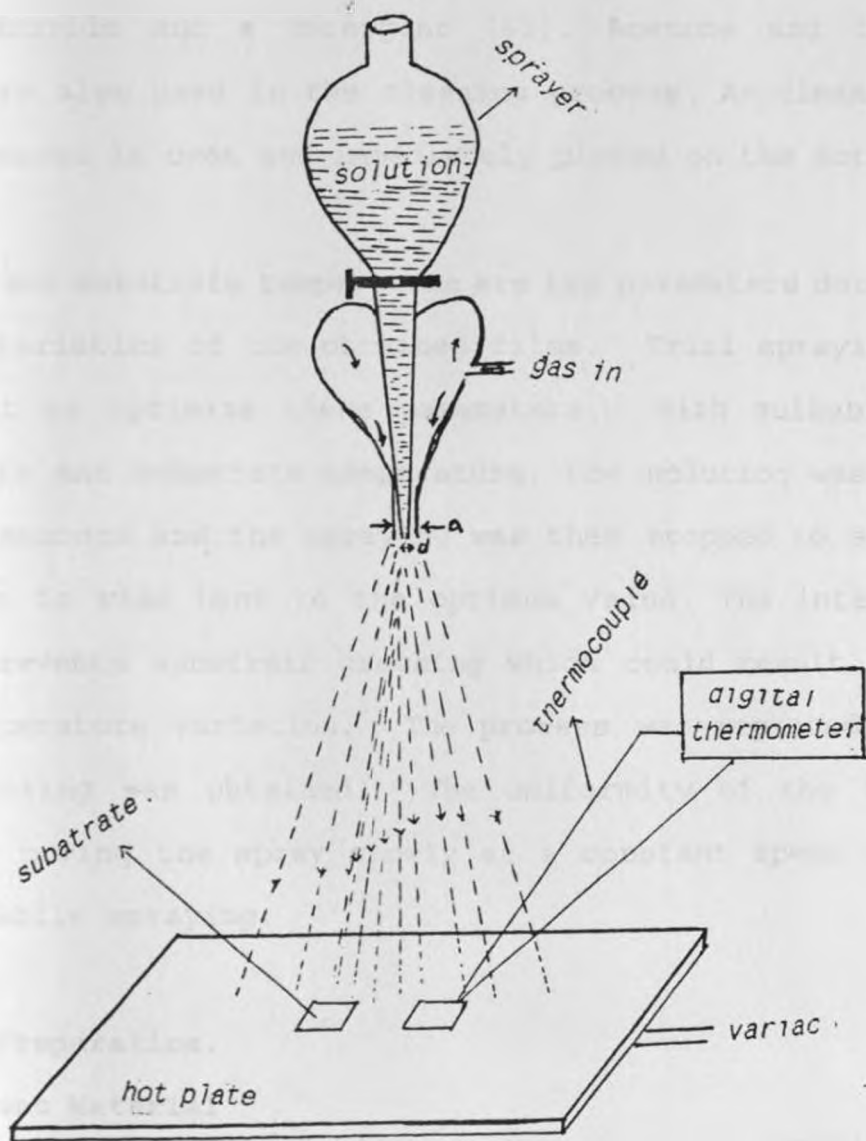


Fig. 3.1. Experimental set-up for spray pyrolysis.

A variac was used to control the plate temperature which was monitored using a copper-nichrome thermocouple attached to a Fluke 2100A digital thermometer.

The substrate - 2.5 cm x 2.5 cm glass slides - were thoroughly cleaned. The cleaning solution was a mixture of aqueous solution of sodium hydroxide and a detergent [63]. Acetone and isopropyl alcohol were also used in the cleaning process. As-cleaned glass slide was dried in oven and immediately placed on the hot plate.

Spray rate and substrate temperature are key parameters determining the characteristics of the obtained films. Trial sprayings were carried out to optimize these parameters. With suitable spray height, rate and substrate temperature, the solution was sprayed for a few seconds and the spraying was then stopped to allow the temperature to rise back to the optimum value. The intermittent spraying prevents substrate cracking which could result from the sudden temperature variation. The process was repeated until a desired coating was obtained. The uniformity of the film was ensured by moving the spray slowly at a constant speed over the substrate while spraying.

3.3. Film Preparation.

3.3.1. Parent Material

The parent material i.e. the spraying solution was obtained by mixing solutions of Iron Chloride (FeCl_3) and thiocarbamide

also called thiourea. Solutions of molarity ranging between 0.01 and 1 were prepared. For a given molarity, the content FeCl_3 : thiourea: distilled water of the spraying mixture was varied according to the volume ratios indicated in Table 3.1.

Table 3.1 Volume ratio of the components of the spraying solution

FeCl_3 : thiourea	FeCl_3 :thiourea: H_2O
0.50:0.50	0.05 : 0.10 : 0.85
0.35:0.70	0.07 : 0.15 : 0.78
0.25:0.75	0.10 : 0.25 : 0.65
0.20:0.80	0.10 : 0.30 : 0.60

3.3.2. Coating

The mixture was sprayed onto glass substrate held at constant temperature. Samples were prepared at temperatures selected between 300°C and 550°C . During the spraying process, the allowed variation of the substrate temperature was $\pm 5^\circ\text{C}$. After deposition, films were removed from the hot plate and cooled at room temperature. Precaution was taken to avoid cracking while removing and cooling.

3.4 Heat Treatment

Thermal sulfidation was done in hermetically sealed container. A certain amount of sulfur was placed in the container. This amount was calculated to get a pressure within the limit of safety in our experiment, and also to ensure maximum absorption by the sample.

The set was placed on a preheated plate or heated at a given rate up to the annealing temperature which was selected in the range 200°C to 350°C. The preliminary trial experiments showed the silica glass as the best sample container because of the reactive nature of sulphur. Each annealing experiment lasted for one or two hours. As-annealed samples were cooled down slowly up to about 30°C before allowing air in the container. Sulfidated films were thereafter washed in carbon disulfide [64] and alcohol. After several trials, heating rates of 5-8°C per minute were chosen and the cooling rate was about 5°C per minute. For all other rates, the films peeled off while heating or cooling. It was observed that the melting point and the boiling point of sulfur were about 140°C and 400°C, respectively.

The ferrous sulfide FeS is known to be the easily obtained phase of Fe_xS_m species [42] and since the experiments were conducted in the atmosphere, FeS and some oxides of iron could be forming rather than the expected iron pyrite. The sulfidation experiments were therefore aimed at transforming FeS and iron oxides into FeS₂ and to enhance the crystallization of the formed FeS₂ film [43].

3.5 Thickness measurement.

Film thickness was determined by the weighing method using the analytical Mettler H10 balance. The weights were taken before and after coating. Each weighing was preceded by a thorough cleaning. Assuming that the films are uniform, the thickness was calculated

using the relationship [67]:

$$t = \frac{\Delta m}{A \times d} \quad (4-1)$$

Where Δm is the increase in the weight, A is the substrate area and $d = 5.02 \text{ g/cm}^3$ is the density of natural pyrite. The reading error in the weight and length were respectively $\pm 0.1 \text{ mg}$ and $\pm 1 \text{ mm}$.

3.6 Crystallographic analysis.

The surface morphology of the films was investigated by JSM-T 100 scanning microscope in reflective mode. X-ray diffraction patterns were used to identify the nature of the films. A Phillips PW 1730 Automated X-ray diffractometer with $\text{CuK}\alpha$ line at 1.54183 \AA was used. The sample was rotated around an axis perpendicular to the monochromatic X-rays beam while recording the intensity of the diffracted radiation as a function of the Bragg angle θ . The lattice parameter d was calculated from the angular position of the peak maxima using Bragg's law:

$$n\lambda = 2d\sin\theta$$

3.7 Optical Transmission.

The transmission of light through the films was measured by a Perkin Elmer 550S UV/Visible spectrophotometer using ratio-recording technique. The scanned wavelength range was 400 nm to 800 nm . Neither UV nor IR ranges could be scanned because glass (substrate) absorbs totally UV radiations and IR spectrophotometer

was not available.

In ratio-recording technique, the transmittance of a thicker film relative to a thinner film is measured. Doing so is equivalent to measuring the transmittance of a hypothetical film of thickness equal to the difference in the thickness of the two films without the reflection losses. In this work, a blank substrate was placed in the reference beam while the film was put in the sample beam. The recorded data - shown in Table 4.1 - were therefore the transmittance of the film. All measurements were carried out at room temperature. A large number of films was studied and reproducible results were obtained.

3.8 Electrical and Hall measurements.

Hall measurement at room temperature were taken to determine the free carrier concentration and the Hall mobility μ_H while the resistivity was measured by the two points probe method. Aluminum was used for ohmic contact. Hall measurements were conducted on samples of resistivities 156 ΩCm and 700 ΩCm . The current I was measured with a Keithly picometer 414A, the Hall voltage was measured with a digital multimeter 1905a and a fluxmeter YEW 3254 was used to measure the magnetic field.

CHAPTER FOUR

RESULTS AND DISCUSSION.

In this chapter, crystallographic, electrical, and optical properties of FeS₂ films, grown by spray pyrolysis are presented and discussed. Effects of annealing and sulfidation on these properties are also presented.

4.1. Some Qualitative Observations.

Films were first analysed visually for uniformity and for any pin holes. It was found that the following deposition parameters give films with shinny smooth surfaces:

- (i) Spray rate 24 cm³/min
- (ii) Distance between sprayer and substrate 35-40 cm
- (iii) Substrate temperature between 450°C and 550°C
- (iv) Mixture content FeCl₃ : thiourea :H₂O in the ratio 0.07:0.15:0.78 if the molarity is in the range 0.1 and 1 and FeCl₃:Thiourea in the ratio 1:2 for molarity less than 0.1.

The films were brownish yellow in color with very good adhesive properties.

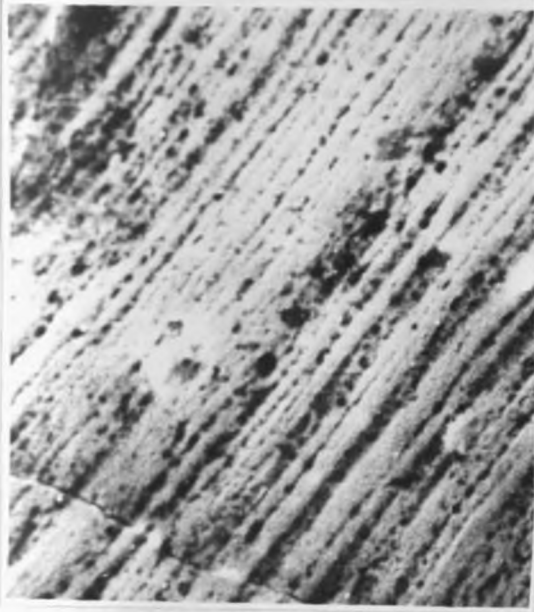
For high spray rates or lower spray heights, the substrate cracked due to rapid cooling. For higher heights, a lot of solution was wasted. For low spray rates or for low substrate temperatures, the droplets falling on the substrate surface could not decompose immediately; black precipitates were left on the surface.

Generally, at lower substrate temperatures, the films became black in color. The black color films obtained at lower substrate temperature i.e. less than 350°C can be related to the formation of the FeS phase [25].

The thickness of the films were found to be in the range of 0.2 to 1.2 μm with estimated errors of at most $\pm 0.08 \mu\text{m}$. However this remain a rough calculation since thin film material has certainly a density different from the one of natural pyrite used here. Again, the balance used in the experiment was not sensitive enough to detect small changes in the weight. Sulfidation treatments may have given rise to an increase in the thickness as a consequence of sulfur adsorption and crystallization. No estimation of such change could be made due to limited perfection of the balance. More accurate thickness measurement can be obtained by methods such as stylus techniques or optical interference. None of these methods could be used due to the lack of appropriate equipments i.e. stylus instrument and IR spectrophotometer.

4.2. The Surface Morphology

Figures 4.1 show scanning electron micrographs of three samples. It took respectively 45 and 70 min. to grow samples in (a) and (b) while sample (c) was grown within less than 20 min. and sulfidated at 350°C.



5 μm

(a)



5 μm

(b)



(c)

1 μm

Fig.4.1 Scanning electron micrographs of some samples.

The photographs (a) and (b) show striated surface. Jerrery [65] reported such structure for a polycrystalline specimen whose major components were Fe_2O_3 , Fe_3O_4 and FeO using selected area diffraction microanalysis. The formation of iron oxides in these two samples can be attributed to annealing effects since it took longer time to grow the films. In fact various oxides can be formed by thermal oxidation upon heating in air; the sulfur escaping in the atmosphere with volatile by-products. A surface morphology similar to the one seen on photograph (c) was reported by Ferrer et al [42] for FeS_2 film obtained by sulfidation of flash evaporated iron film and by Ennaoui et al [44] for FeS_2 film prepared by epitaxial growth.

4.3. Crystallographic Properties.

Figure 4.2 shows X-ray diffraction patterns of as grown film (a) and after sulfidation (b). The diffractograph of a natural sample is also shown (c).

As-deposited film showed amorphous phase. Annealing in air ambient or vacuum did not improve the crystallinity. Presence of FeS_2 can be concluded from Fig. 4.2(b). A dominant peak (200) corresponding to the d-spacing 2.71 Å and indicating the existence of preferred orientation in (200) direction can be seen. The (200) peak is the second highest in a natural sample. A look at S and FeS cards on ASTM index shows that (200) peak does not appear in X-ray diffraction patterns of S while it is the lowest in FeS patterns.

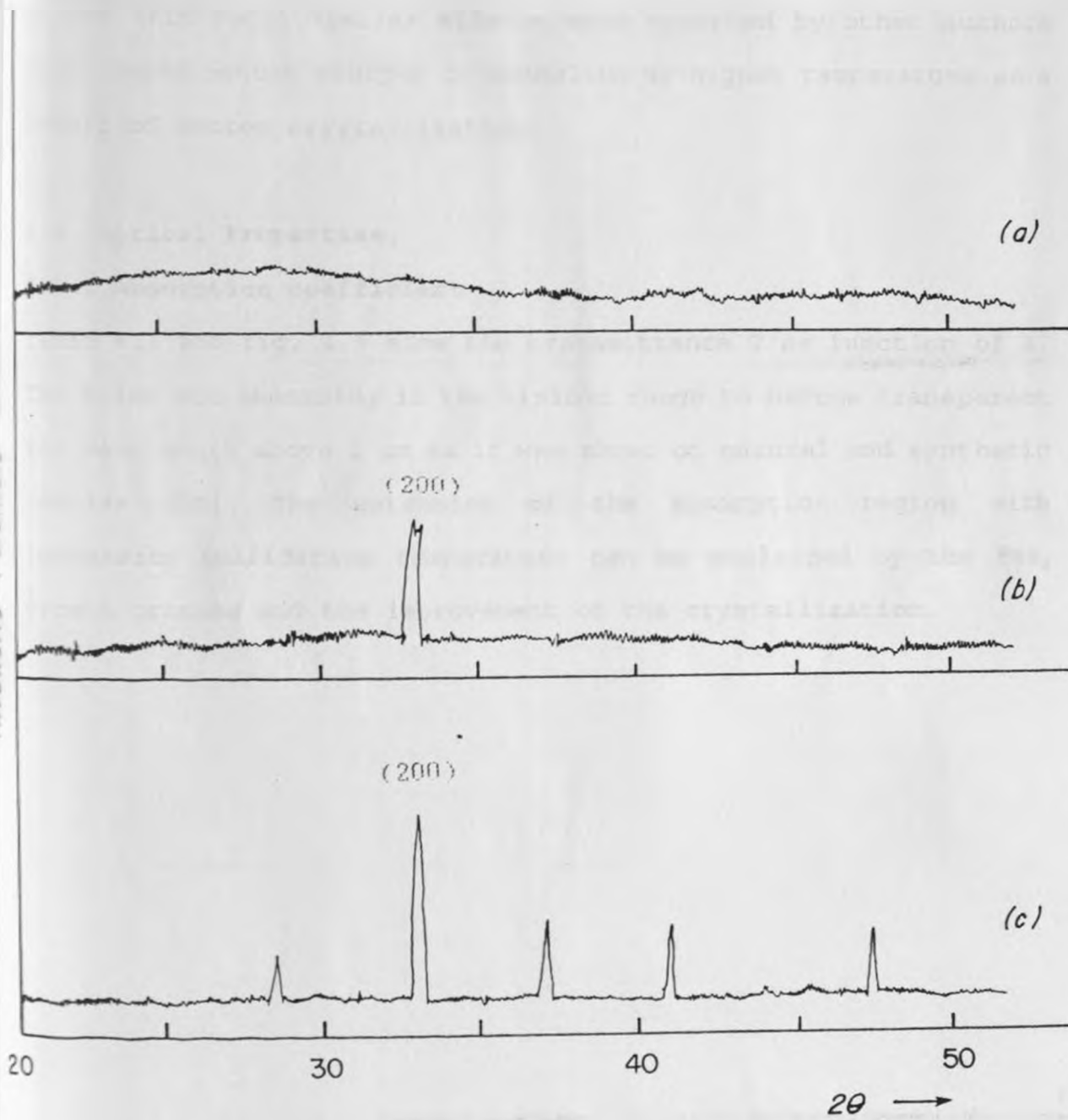


Fig.4.2 X-ray diffractograph of (a) as deposited, (b) sulfidated at 350°C films and (c) a natural iron pyrite.

It can therefore be concluded that no sulfur was present in our films although some FeS might appear in small proportion. In fact the peak in Fig. 4.2(b) is a triplet suggesting some transformation of FeS into FeS₂. Similar effects were reported by other authors [42]. Peaks become sharper on annealing at higher temperature as a result of better crystallization.

4.4. Optical Properties.

4.4.1 Absorption coefficient

Table 4.1 and fig. 4.3 show the transmittance T as function of λ . The films are absorbing in the visible range to become transparent for wavelength above 1 μm as it was shown on natural and synthetic samples [24]. The extension of the absorption region with increasing sulfidation temperature can be explained by the FeS₂ growth process and the improvement of the crystallization.

Table 4.1 Transmittance as function of wavelength for films of thickness $0.5 \pm 0.08 \mu\text{m}$, substrate and sulfidation temperatures respectively (a) 500°C and no sulfide. (b) 550°C and 250°C , and (c) 500°C and 350°C .

λ (μm)	$h\nu$ (eV)	T %		
		(a)	(b)	(c)
0.40	3.1	2.4	0.0	0.0
0.45	2.9	7.5	0.0	0.0
0.50	2.5	15.0	0.7	0.1
0.55	2.3	25.0	2.2	0.7
0.60	2.1	37.0	11.8	1.3
0.65	1.9	44.3	17.8	2.1
0.70	1.8	48.0	20.7	3.5
0.75	1.7	50.2	29.0	7.1
0.80	1.6	52.1	33.7	15.9

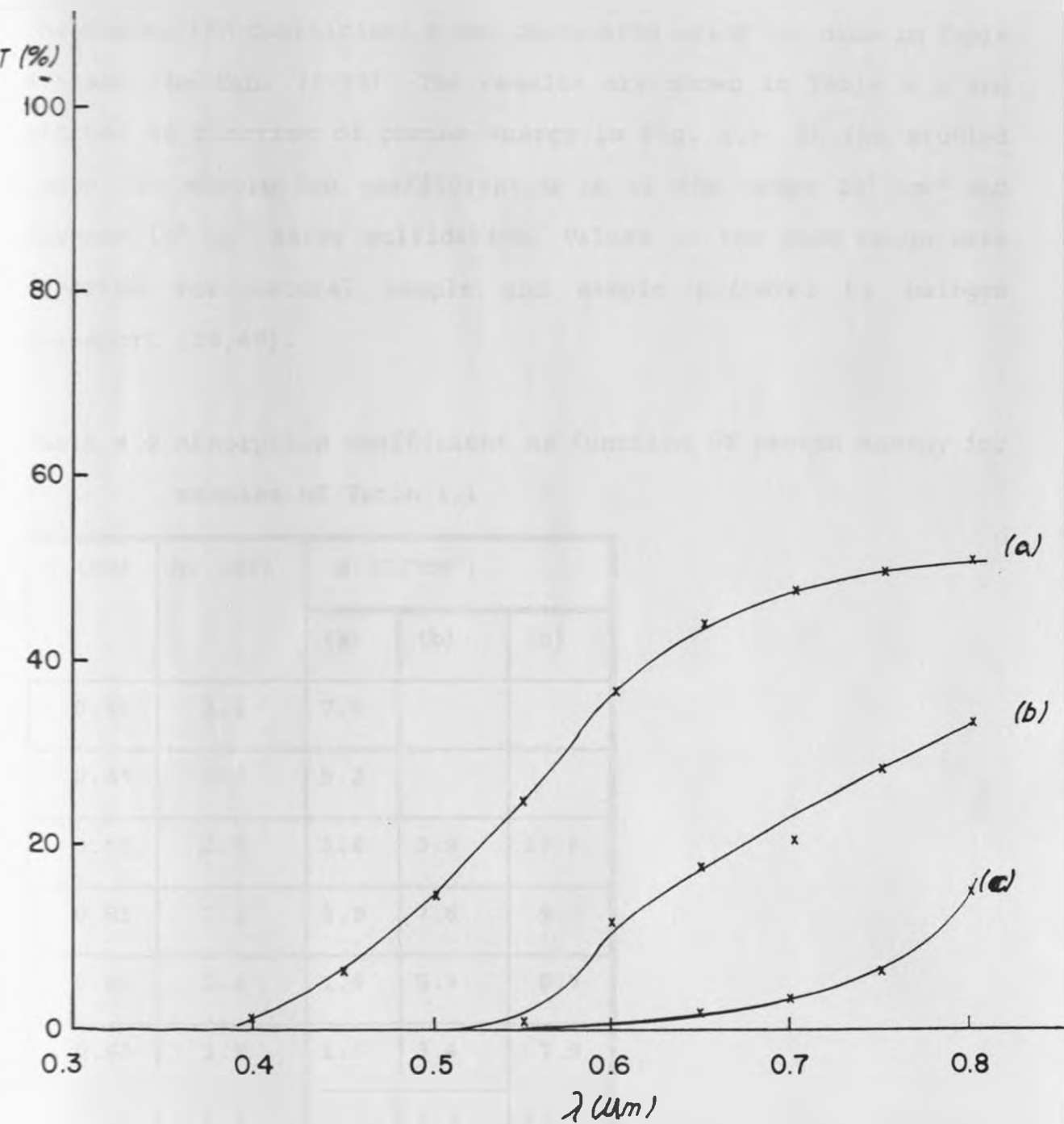


Fig. 4.3 Transmission spectra for (a) as deposited, (b) sulfidated at 250°C and (c) at 350°C films.

The absorption coefficient α was calculated using the data in Table 4.1 and the Eqn. (2-19). The results are shown in Table 4.2 and plotted as function of photon energy in Fig. 4.4. In the studied range the absorption coefficient α is of the order 10^4 cm^{-1} and reaches 10^5 cm^{-1} after sulfidation. Values in the same range were reported for natural sample and sample prepared by halogen transport [39,40].

Table 4.2 Absorption coefficient as function of photon energy for samples of Table 4.1

λ (μm)	$h\nu$ (eV)	α (10^4 cm^{-1})		
		(a)	(b)	(c)
0.40	3.1	7.5		
0.45	2.9	5.2		
0.50	2.5	3.8	9.9	13.8
0.55	2.3	2.9	7.6	9.9
0.60	2.1	1.9	5.3	8.7
0.65	1.9	1.6	3.4	7.9
0.70	1.8	1.5	3.1	6.7
0.75	1.7	1.4	2.5	5.3
0.80	1.6	1.3	2.2	3.7

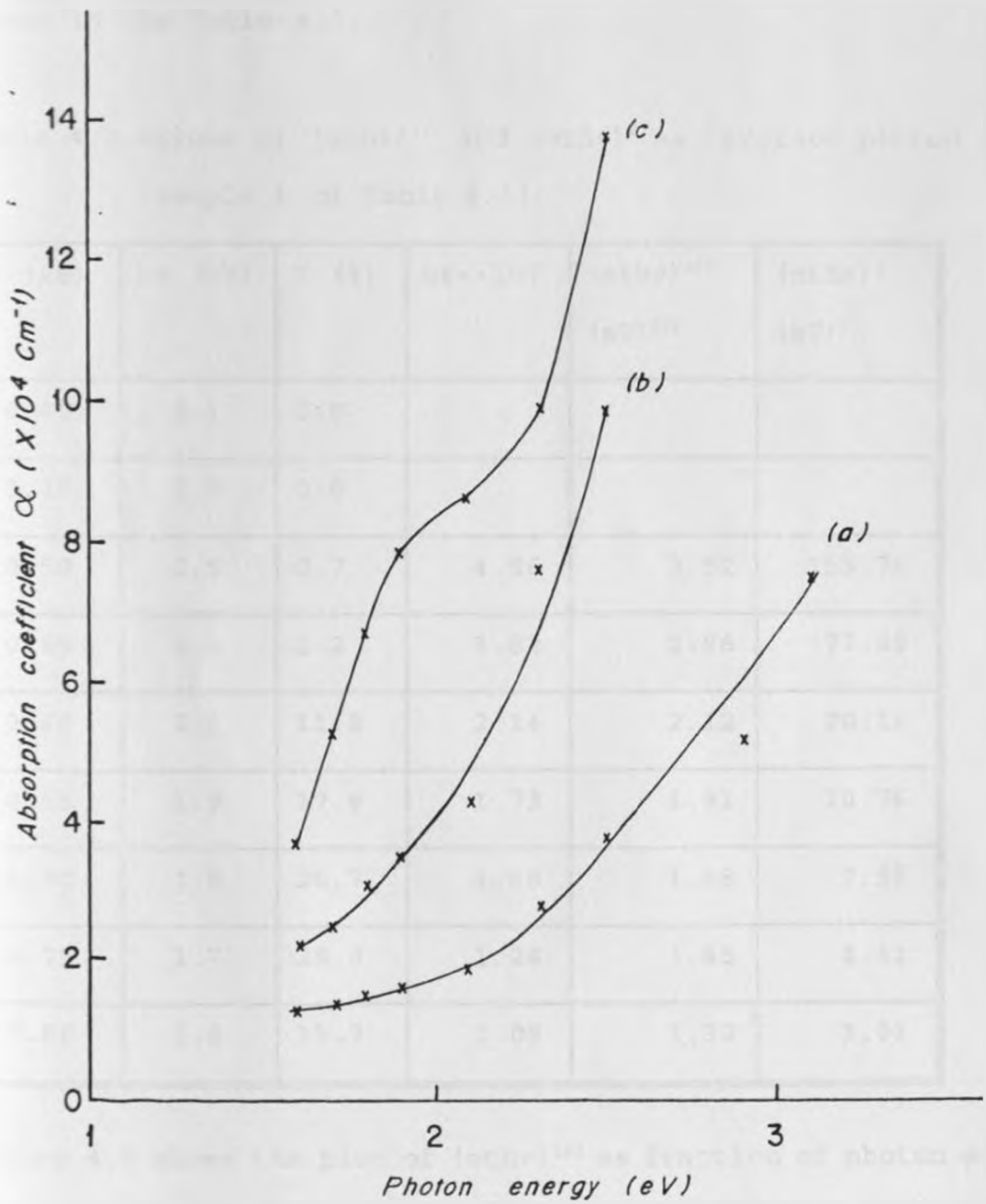


Fig. 4.4 The absorption coefficient as function of photon energy for samples of figure 4.3.

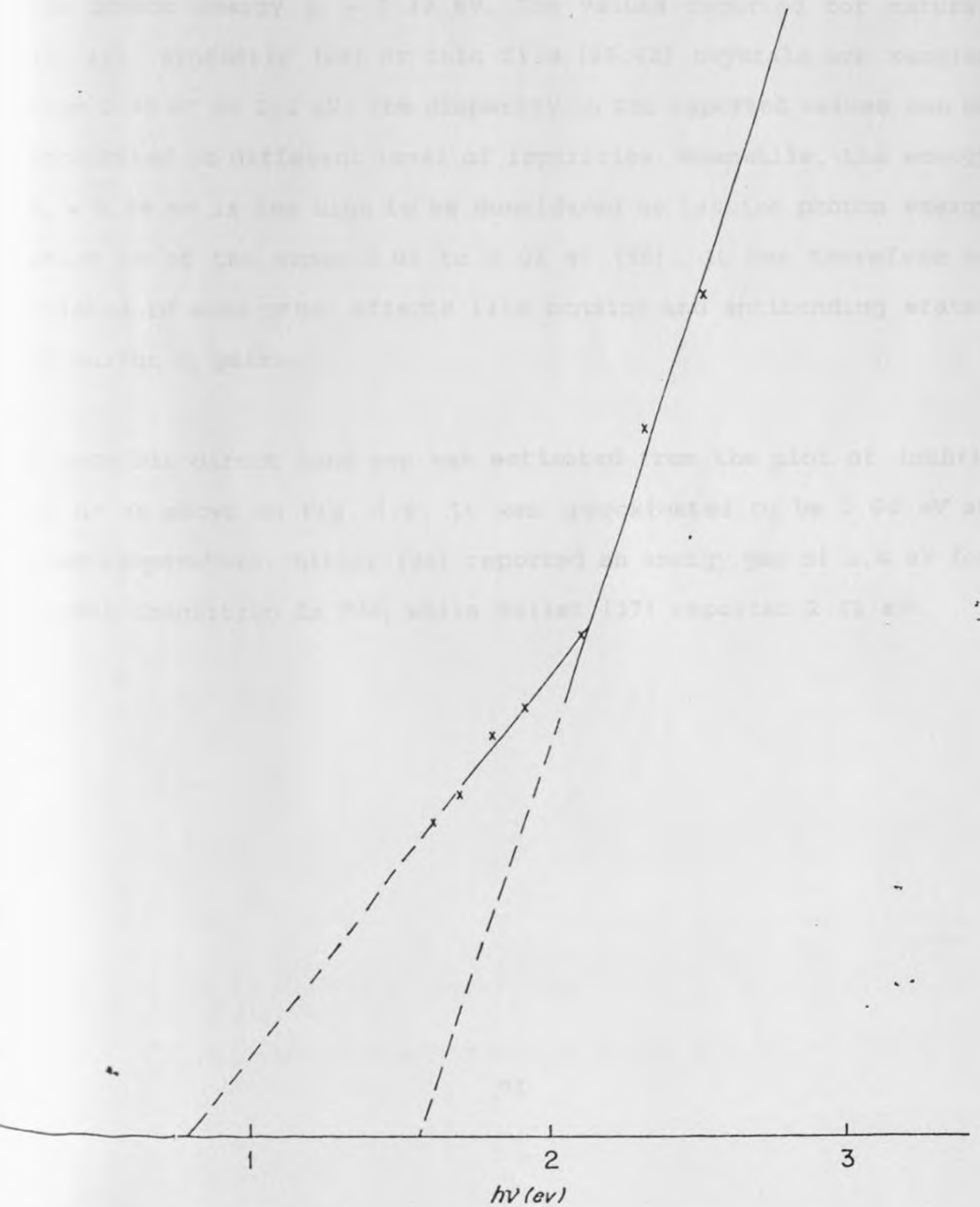
4.4.2 Energy Band Gap

The indirect band gap was estimated from the plot of $(\alpha h\nu)^{1/2}$ vs $h\nu$ as explained in section 2.9. The details of the calculation are shown in the Table 4.3.

Table 4.3 Values of $(\alpha h\nu)^{1/2}$ and $(\alpha h\nu)^2$ as function photon energy (sample b of Table 4.1)

λ (μm)	$h\nu$ (eV)	T (%)	$\alpha t = -\ln T$	$(\alpha h\nu)^{1/2}$ (eV) ^{1/2}	$(\alpha h\nu)^2$ (eV) ²
0.40	3.1	0.0			
0.45	2.9	0.0			
0.50	2.5	0.7	4.96	3.52	153.76
0.55	2.3	2.2	3.82	2.96	77.09
0.60	2.1	11.8	2.14	2.12	20.16
0.65	1.9	17.8	1.73	1.81	10.76
0.70	1.8	20.7	1.58	1.68	7.95
0.75	1.7	29.0	1.24	1.45	4.41
0.80	1.6	33.7	1.09	1.32	3.03

Figure 4.5 shows the plot of $(\alpha h\nu)^{1/2}$ as function of photon energy. Two straight line portions are obtained. The straight line obtained at lower photon energy corresponds to phonon absorption and the



E. 4.5. Plot of $(\alpha h\nu)^{1/2}$ as a function of the photon energy.

intercept on the energy axis occurs at $E_g - E_p \approx 0.78$ eV. The other line arises from transitions involving emission of phonons and the corresponding intercept occurs at $E_g + E_p \approx 1.56$ eV.

The two intercepts give the indirect energy gap $E_g \approx 1.17$ eV and the phonon energy $E_p \approx 0.39$ eV. The values reported for natural [37-40], synthetic [24] or thin film [25,42] crystals are ranging from 0.95 eV to 1.2 eV. The disparity in the reported values can be attributed to different level of impurities. Meanwhile, the energy $E_p \approx 0.39$ eV is too high to be considered as lattice phonon energy which is of the order 0.01 to 0.03 eV [55]. It can therefore be related to some other effects like bonding and antibonding states of sulfur S_2 pairs.

A possible direct band gap was estimated from the plot of $(\alpha h\nu)^2$ vs $h\nu$ as shown in Fig. 4.6. It was approximated to be 2.60 eV at room temperature. Bither [24] reported an energy gap of 2.4 eV for direct transition in FeS_2 while Bullet [37] reported 2.62 eV.

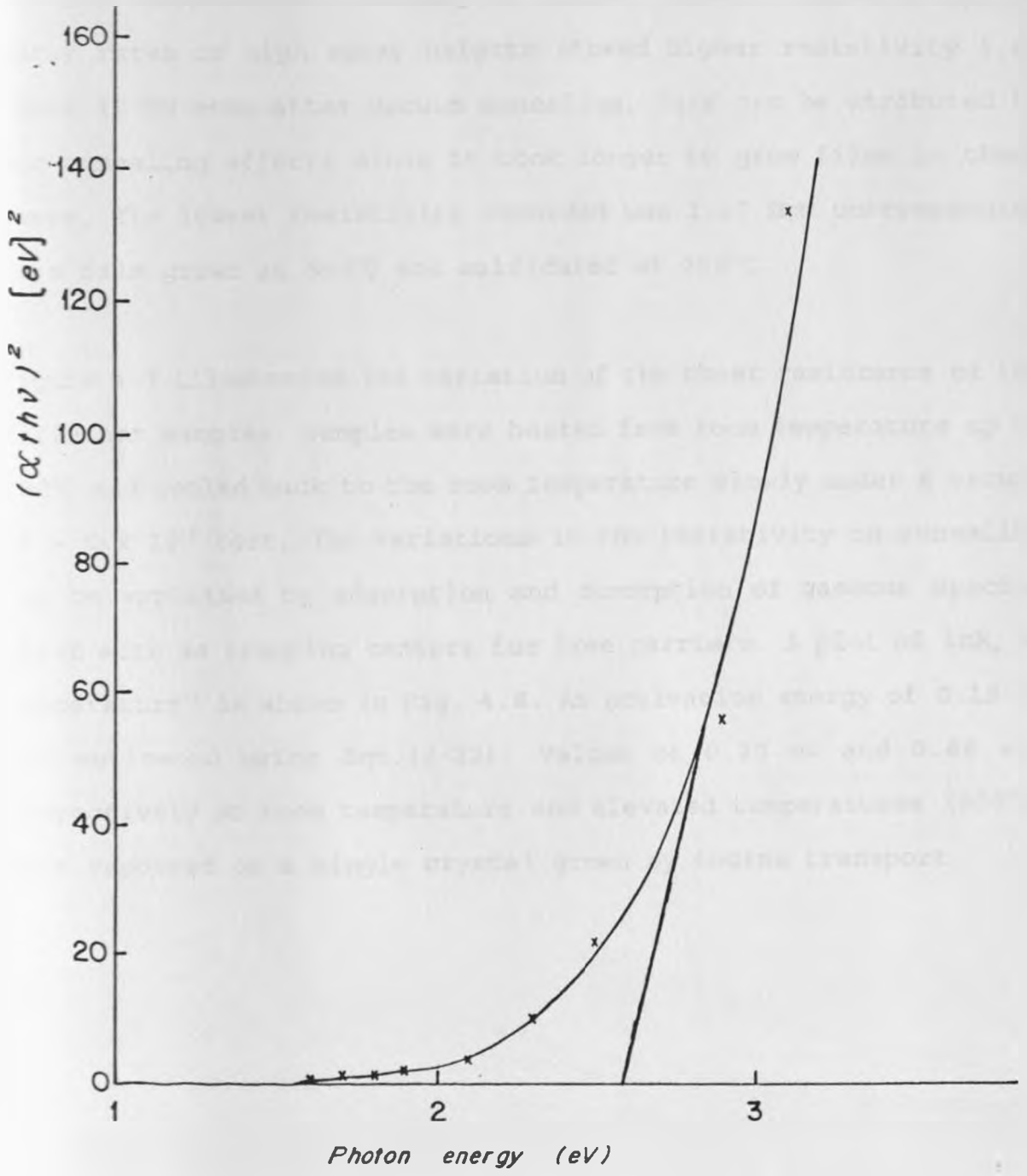


Fig. 46 Plot of $(\alpha h\nu)^2$ as a function of the photon energy.

4.5. Electrical Properties.

4.5.1 Temperature variation of resistivity

It was observed that sheet resistivity increases on annealing in air and decreases on annealing in vacuum. Films obtained using low spray rates or high spray heights showed higher resistivity i.e. above 20 M Ω even after vacuum annealing. This can be attributed to air annealing effects since it took longer to grow films in these cases. The lowest resistivity recorded was 1.17 Ω cm corresponding to a film grown at 550°C and sulfidated at 250°C.

Figure 4.7 illustrates the variation of the sheet resistance of two different samples. Samples were heated from room temperature up to 190°C and cooled back to the room temperature slowly under a vacuum of $\approx 6 \times 10^{-5}$ torr. The variations in the resistivity on annealing can be explained by adsorption and desorption of gaseous species which acts as trapping centers for free carriers. A plot of $\ln R_s$ vs temperature⁻¹ is shown in Fig. 4.8. An activation energy of 0.19 eV was estimated using Eqn. (2-22). Values of 0.20 eV and 0.46 eV, respectively at room temperature and elevated temperatures (500°K) were reported on a single crystal grown by iodine transport.

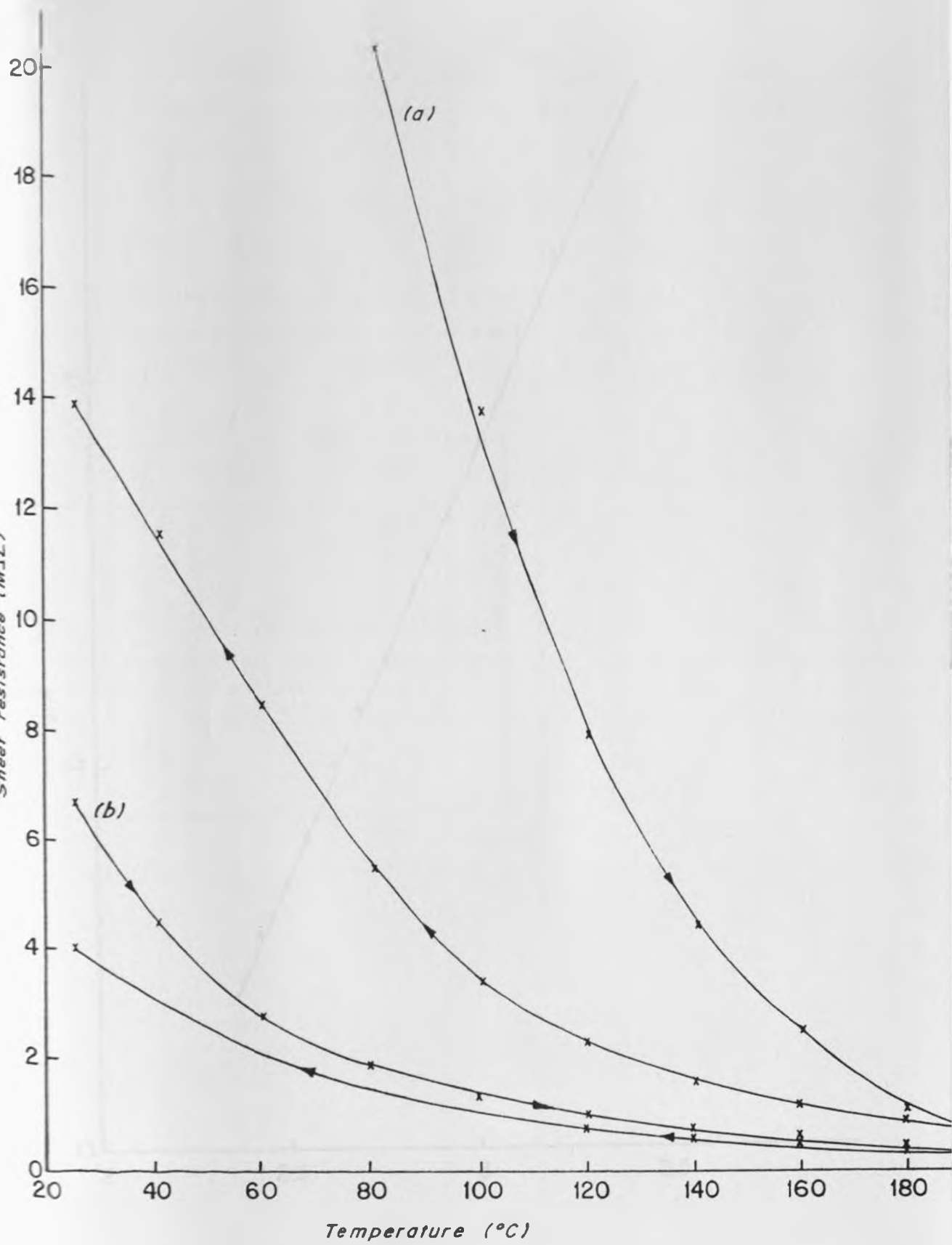


Fig. 4.7 Sheet resistance as function of temperature.

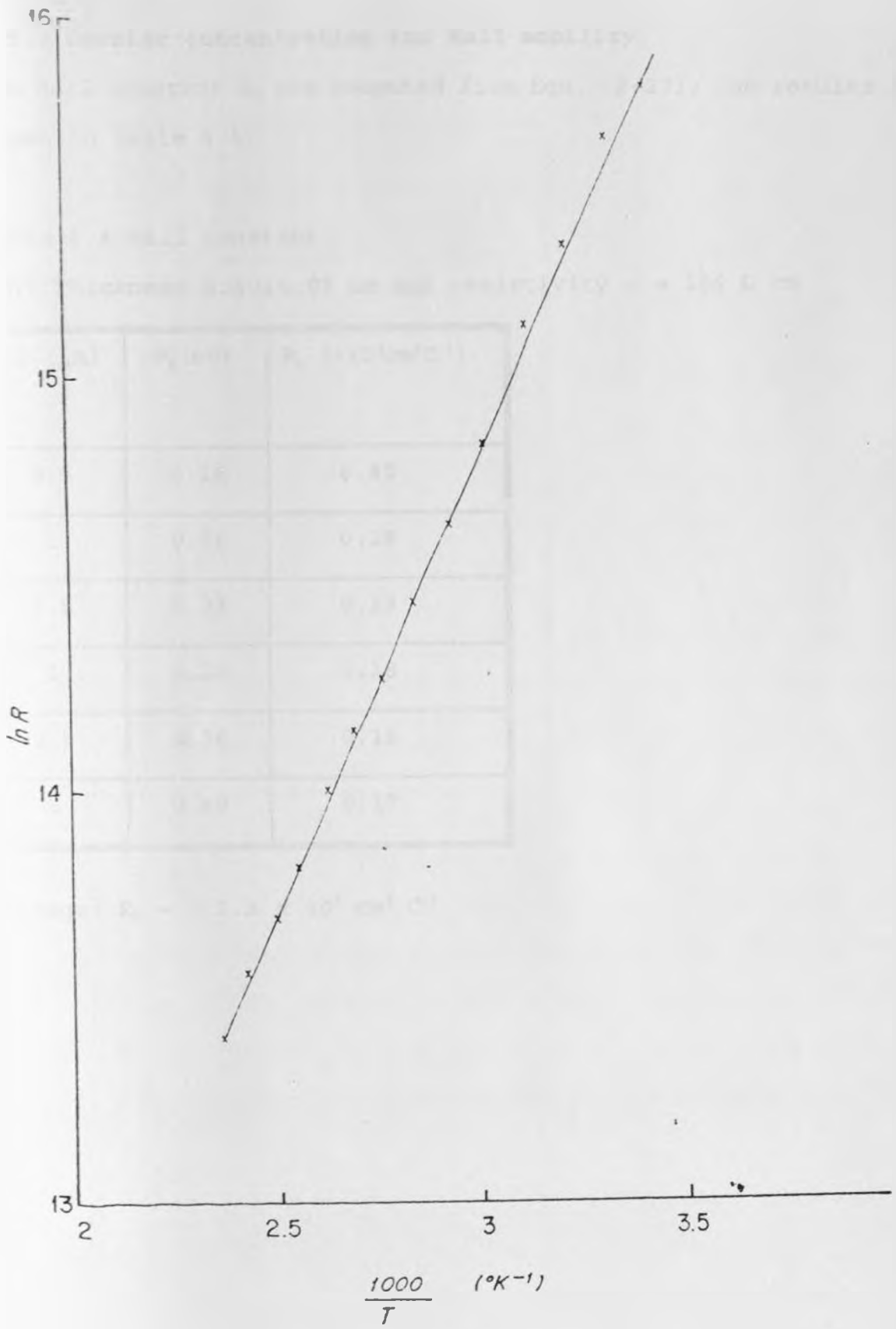


Fig. 4.8. Plot of $\ln R_s$ as function of temperature⁻¹.

4.5.2 Carrier concentration and Hall mobility

The Hall constant R_H was computed from Eqn. (2-27); the results are shown in table 4.4.

Table 4.4 Hall constant.

(a) Thickness $0.39 \pm 0.08 \mu\text{m}$ and resistivity $\rho = 156 \Omega \text{ cm}$

I (μA)	$-V_H$ (mV)	R_H ($-10^3 \text{cm}^3 \text{C}^{-1}$)
0.5	0.16	0.40
1	0.20	0.25
1.5	0.23	0.19
2	0.28	0.18
2.5	0.36	0.18
3	0.40	0.17

Average: $R_H = - 2.3 \times 10^2 \text{ cm}^3 \text{ C}^{-1}$

(b) Thickness $0.50 \pm 0.08 \mu\text{m}$ and resistivity $750 \Omega\text{cm}$

I (μA)	$-V_H$ (mV)	R_H ($-10^3 \text{ cm}^3 \text{ C}^{-1}$)
0.1	0.032	0.40
0.2	0.068	0.43
0.3	0.103	0.43
0.4	0.134	0.42
0.5	0.168	0.42
0.6	0.203	0.42
0.7	0.241	0.43
0.8	0.280	0.44
0.9	0.305	0.42

Average: $R_H = -4.2 \times 10^2 \text{ cm}^3 \text{ C}^{-1}$

The carrier concentration n and the Hall mobility μ_H were calculated using the Eqns. (2-28) and (2-29); the results are shown in the Table 4.5. From the negative sign of the Hall constant, it can be concluded that the films exhibit n-type conduction.

Table 4.5 R_H , n and μ_H for two samples of different resistivities.

ρ (Ω cm)	R_H (10^2 cm ³ C ⁻¹)	n (10^{17} cm ⁻³)	μ_H (cm ² V ⁻¹ s ⁻¹)
156	- 2.3	0.23	1.5
700	- 4.2	0.15	0.6

The Hall mobility in our samples is quite low. This can be explained by impurity and lattice imperfection scattering. Ennaoui [32] reported a carrier concentration of 3×10^{17} cm⁻³ and a Hall mobility of 3 cm²V⁻¹s⁻¹. A highest mobility of 230 cm²V⁻¹s⁻¹ has been reported by Bither [24].

CHAPTER FIVE

CONCLUSION AND SUGGESTIONS FOR FUTURE WORK

5.1 Conclusion.

Iron pyrite FeS_2 films have been grown on glass substrate by spray pyrolysis followed by sulfidation. The deposition parameters were identified and their optimum values determined. These values were found to be; substrate temperature between 450°C and 550°C , spray height 35 to 40 cm and spray rate $24 \text{ cm}^3/\text{min}$. The volume ratio of the spraying mixture contents FeCl_3 : thiourea : H_2O which gave the best films were found to be 0.07 : 0.15 : 0.78 if the molarity is in the range of 0.1 to 1 and, 1 : 2 for molarity less than 0.1. Films obtained in these conditions were highly transparent, with smooth surfaces and very good adhesive properties. The thickness of the films were in the range of 0.2 to $1.2 \pm 0.08 \mu\text{m}$.

As-deposited films were annealed in sulfur vapor at temperatures varying between 200°C and 350°C . From X-ray diffraction and scanning electron microscopy, it was observed that the sulfidation favour the transformation of as-deposited films into FeS_2 and improved the crystallization of the films. The films showed a preferred orientation in the (200) direction.

The electrical properties and the effects of annealing on these properties were investigated. As-deposited films showed high sheet resistance i.e. in the order of $20 \text{ M}\Omega/\square$. Annealing in air increased

the sheet resistivity while it decreased on annealing in sulfur atmosphere or in vacuum.

The lowest resistivity recorded was $\rho = 1.17 \Omega\text{cm}$ for a sample of sheet resistance $300 \text{ k}\Omega/\square$ and $0.39 \mu\text{m}$ thick. An activation energy of 0.19 eV was estimated in the temperature range 25°C to 180°C . The relatively high sheet resistance can be explained by the resistance at the ohmic contacts, the purity of the chemical used, the adsorption of gaseous species during the deposition process, the porosity of the films, etc.

The Hall measurement with a magnetic field of 4 kilogauss gave the Hall constant R_H between -4.2 and $-2.3 \times 10^{-3} \text{ cm}^3\text{C}^{-1}$, the carrier concentration in the range 0.15 and $0.23 \times 10^{17} \text{ cm}^{-3}$ and the Hall mobility μ_H between 0.6 and $1.5 \text{ cm}^2\text{V}^{-1}\text{s}^{-1}$. The variation in these constants can be explained by the different levels of the impurities in the samples. The negative sign of the constant R_H confirmed that the films were n-type.

The optical transmission data were analysed to investigate the energy gap and the absorption coefficient of the films. An indirect energy gap of 1.17 eV , a possible direct energy gap of 2.60 eV and an absorption coefficient $\sim 10^4$ to 10^5 cm^{-1} were found. The absorption coefficient increased with the annealing temperature.

The spray pyrolysis is a simple and inexpensive technique for thin film deposition since the set up uses materials locally available. But the properties of films produced by this technique are strongly influenced by the complexity of the environment in which the coating is carried out. The main difficulties are to ensure the coherence and the uniformity of the film and also to avoid contamination during the deposition and the evolution of dangerous gaseous by-products.

5.2 Suggestions for Future Work.

During the course of the experiments, several observations which could lead to the improvement of the films crystallinity and to the increase of the carriers mobility have been made.

In the experiments, 98 % pure chemicals - the only one available and affordable on the local market - were used. We believe that stoichiometric ratio closer to the one of FeS_2 , can be achieved by using highly pure chemicals.

The contamination risk can be reduced if a better control of the environment in which the growth occurs is ensured. The spraying should be done in a closed medium while evacuating the gaseous by-products; which means a better control not only of the substrate temperature but also of the spraying chamber pressure. The cleaning process needs also to be improved.

More work should be done on determining the optimum conditions for FeS_2 film deposition. A system moving the sprayer at constant speed while spraying should be designed. Deposition onto crystalline substrate such as quartz plate and natural pyrite should be investigated. Such substrate offers the advantage of a pre-existing crystalline structure on which a new one can easily be built. Also quartz has a very small expansion coefficient and therefore film cracking can be avoided.

Thermal sulfidation appeared to be important to improve the crystallinity of as-deposited films on glass substrate. Therefore, the effects of sulfidation duration, temperature and of the sulfur pressure on the properties of the films needs to be thoroughly investigated. Considering the reactive nature of the sulfur, the experiments should be carried out in vacuum sealed glass ampoule, provided with appropriate means of measuring temperature and sulfur pressure.

REFERENCES.

1. S.W.Angrist, **Direct Energy Conversion**, 4th ed., Allyn and Bacon, Inc, Boston, 9(1982).
2. C.G.Grangrist (Editor), **Materials science for solar energy conversion systems**, Pergamon press plc., Oxford, 1 (1991).
3. T.Markvart (Editor), **Solar Electricity**, John Willy and Sons Ltd, Delhi, 1(1994).
4. M.Ghanam , in: **Prosseding of a college on thin film technology**, vol.4, Dar es Salaam (1994); unpublished.
5. K.V.O.Rabah, L.Ndjeli and A.K.Raturi, Internat. Atomic Energy Agency/internal report: **Review of photovoltaic energy development in Kenya for rural electrification**, Miranare Trieste, (1995).
6. D.C.Card and H.C.Card, **Solar Energy** 28(6), 451 (1982).
7. A.J.Nozik, **J.of Crystal Growth** 39, 200 (1977).
8. S.Kar, K.Rajeshwar, P.Singh and J.Dubow, **Solar Energy** 23, 129 (1979).
9. L.Stuart, H.Gary, T.Reshef and M.Joast, **Nature** 326, 863 (1987).
10. H.Gerischer, **J.Electroanal.Chem.**82, 115 (1977).
11. A.Heller, **Solar Energy** 29(2), 153 (1982).
12. K.L.Stevenson and W.F.Erbelding, **Solar Energy** 27(2), 139 (1981)
13. B.O'Regan and M.Gratzel, **Nature** 353, 737 (1991).
14. J.O.M.Bockris and S.Srimivassan, **Fuel cells: their electrochemistry**, McGrawHill, New York, 50 (1969).

15. H.Tributsch, in: **Structure and Bonding** (C.K.Jorgensen, ed.), vol.49, Springer-Verlay Berlin Heidelberg, 127-175 (1982).
16. S.M.Sze, **Physics of Semiconductor Devices**, Willey Inter Sc., NY, (1969).
17. A.Hagfeldt, U.Bjorksten and S.E.Lindquist, **Solar Energy Materials and Solar Cells** **27**, 293 (1992).
18. A.Hagfeldt, B.Ddrikson, T.Palmqvist, H.Lindstron, S.Sodergren, H.Rensmo, and S.E.Lindquist, **Solar Energy Materials and Solar Cells** **31**, 481 (1994).
19. S.Sodergren, A.Hagfeldt, J.Olsson and S.E.Lindquist, **J.Phys.Chem.****98**, 5552 (1994).
20. H.J.Lewerenz, A.Heller, and F.J.Disalvo, **J. Am. Chem. Soc.****102**(6), 1877(1980).
21. A.J.Nozik, **Ann. Rev. Phys. Chem.** **29**, 189 (1978).
22. J.A.Wilson and A.D.Yoffee, **Adv.in Phys.****18**(73), 193 (1969).
23. R.M.Candea and P.Stetiu, **Solar Energy** **29**(5), 435 (1982).
24. T.A.Bither, R.J.Bouchard, W.H.Cloud, P.C.Donohue and W.J.Siemons, **Inorg.Chem.****7**(11), 2208 (1968).
25. A.M.Karguppikar and A.G.Vedeshar, **Phys.Stat.Solidi** **A95**, 717 (1986).
26. L.F.Schnemeyer and M.S.Wrighton, **J.Am.Chem.Soc.****101**(22), 6496 (1979).
27. F.F.Fan, H.S.White, B.L.Wheeler and A.J.Bard **J.Am.Chem.Soc.****102**(16), 5142 (1980).
28. L.F.Schenemeyer and M.S. Wrighton, **J.Am.Chem.Soc.****102**(23), 6964 (1980).

29. A.Marina, C.Fulvio, G.Pierluigi and S.Maurizio, *J.Am.Chem.Soc.* **102**(22), 6898 (1980).
30. H.Gerischer, *Electrochem. Acta* **35**, 16677 (1990).
31. L.F.Mattheiss, *Phys.Rev.***B8**(8), 3719 (1973).
32. A.Ennaoui, S.Fiecher, H.Goslowsky and H.Tributsch, *J. Electrochm. Soc.*, vol **132**(7) 1579 (1985).
33. A.Ennaoui and H.Tributsch, *J.Electroanal.chem.*, vol **204**, 185 (1986).
34. A.Ennaoui and H.Tributsch, *Solar Energy Materials* **14**, 461 (1986).
35. K.Sato, *J.Phys.Soc.Jpn* **53**(5), 1617 (1984).
36. L.Grossman, **McGraw-Hill Encyclopadia of Science and Technology** vol., 6th ed., McGraw-Hill Book Company, USA, 495(1987).
37. D.W.Bullet, *J.Phys.C: Solid State Phys.***15**(30), 6163 (1982).
38. J.C.Marinace, *Phys.Rev.*2nd Series **96**(3), 593 (1954).
39. A.Schlegel and P.Wachter, *J.Phys.C: Solid State Phys.***9**(17), 3363 (1976).
40. W.Kou and M.S.Seehra, *Phys.Rev.***B18**(12), 7062 (1978).
41. H.Horita, *J.Phys.Soc.Jpn* **33**(6), 1723 (1972).
42. J.Ferrer and C.Sanchez, *J.Appl.Phys.***70**(5), 2641 (1991); and Ref.therein.
43. G.Smestad, A.Ennaoui, S.Fiechter, H.Tributsch, W.K.Hofmann, M.Birkholz and W.Kautek, *Solar Energy Materials* **20**, 149 (1990).
44. A.Ennaoui, G.Schlichthorl, S.Fiechter, H.Tributsch, *Solar Energy Materials and Solar Cells*, **25**, 169 (1992)

45. F.A.Cotton and G.Wilkinson, *Advanced inorganic chemistry*, Willey Eastern Ltd, New Delhi (1993).
46. W.M.Manyonge, *Technological development of ceramic CdS/Cu₂S solar cell*, MSc.thesis, Univ. of Nairobi (1981); unpublished.
47. B.O.Ogola, *Fabrication and characterization of silicon solar cells*, MSc.thesis, Univ. of Nairobi (1985); unpublished.
48. N.V.Kalaiya, *Fabrication of a semiconductor insulator semiconductor photovoltaic converter*, MSc thesis, Univ. of Nairobi (1990); unpublished.
49. M.Mwabora, *Fluorine doped tin oxide by simple chemical vapor deposition*, MSc thesis, Univ. of Nairobi (1992); unpublished.
50. G.O.Amolo, *Properties of thin ZnO films prepared by atmospheric pressure chemical vapor deposition*, MSc thesis, Univ.of Nairobi (1994); unpublished.
51. W.K.Njoroge, *Sprayed Aluminum doped Zinc oxide thin films for solar application as window material for solar cells*, MSc thesis, Univ.of Nairobi (1994); unpublished.
52. J.L.Vossen and W.Kern (Editors), *Thin Film Processes*, Academic Press, Inc, New York, 276 (1978).
53. C.A. Neugebauer, J.B. Newkirk and D.A. Vermilyea (editors), *Structure and properties of thin films*, John Wiley and sons, Inc., New York, (1959).
54. G. Hass (Editor), *Physics of Thin Films*, vol.1, Acad.Press, Inc., New York, (1963).
55. C.Kittel, *Introduction to Solid State Physics*, 5thed., Willey Eastern, New Delhi, (1976).

55. A.Witurouw and F. Spaeper, *J. Appl. Phys.* 75 (3), 1456 (1994).
57. J.M.Ziman, **Electrons and Phonons**, Oxford Univ.Press, London, (1967).
58. J.Friedel, **Dislocations**, Addison-Wesley, (1964).
59. H.Clark, **Solid State Physics**, Macmillan, New York, (1968).
60. R. T. Kivaisi and M. M. Mwamburi, **3rd College on Thin Film Technology: College Proceeding**, Univ. of Dar es Salaam, (1994); unpublished.
61. J. D. Jackson, **Classical Electrodynamics**, 2nd ed., Willy, New York, 1975.
62. J.Millman and C.C.Halkias, **Electronic Devices and Circuits**, Tata McGrae-Hill, New Delhi, 1993.
63. M. Levy and M. P. Sarachik, *Rev. Sc. Instrument* 60(7), 1342 (1989).
64. R. C. Weast and S. Selby (Editors), **Handbook of Chemistry and Physics**, 48th ed., Chem. Rubber Publ. co., Ohio, 1968.
65. A. Engstrom, V. Cosslett and H. Pattee (Editors), **Proc. of the Second Internat. Symposium on X-ray Microscopy and x-ray Analysis**, Amsterdam, pp.446-458 (1960).
66. N. Khare, G. Razzini and L. P. Bicelli, *Thin Solid Film* 185, 113 (1990).
67. R.T. Kivaisi, in: **Prosseding of a College on Thin Film Technology**, vol.1, Dar es Salaam (1994); unpublished.